Universitat Autònoma de Barcelona

PhD Thesis 2017

Synthesis and Characterization of Magnetic Nanocomposites and Their Applications Study

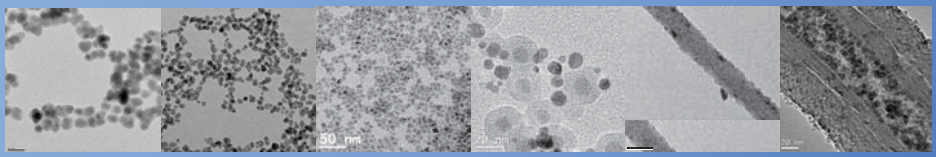

Author: Changyong Lu

Supervised by:

Prof. Josep Ros Badosa

Dr. Susagna Ricart Miro

PhD. Program in Materials Science

Chemistry Department-UAB

ICMAB

CSIC

3.2 Novel Fe_3O_4@GNF@SiO_2 nanocapsules fabricated through the combination of an *in situ* formation method and SiO_2 coating process for magnetic resonance imaging

The tubular property of hollow graphitized nanofibers (GNF) would be promising for encapsulating nanomaterials because of the relative large inner diameter compared with carbon nanotubes. Although, several strategies have been employed to load the inner cavities of carbon nanostructures, regardless of the method employed, bulk filling typically results in samples that contain non-encapsulated material external to the walls and the procedures to remove this external material will always lead to the leakage of the nanomaterials inside the cavities. On the other hand, the open-end structure will bring disadvantages in further applications for example corrosion to the loaded nanomaterials when using the composites under corrosive environment.

In this paper, the in-situ synthesis of Fe_3O_4 nanoparticles inside the cavities method was combined with GNF and the SiO_2 coating process to fabricate novel Fe_3O_4@GNF@SiO_2 nanocapsules. The hybrid materials present a complete filling of the inner GNF cavities with magnetite nanoparticles, which in turn are sealed with a protective SiO_2 coating. The TEM study indicated the successfully formation of nanoparticles inside the cavity, the hybrids synthesized via normal solvent thermal method presence fully filled morphology. Due to the presence of the silica layer, the obtained nanocapsules still present a good magnetic response even after an acid treatment. It is also worth

to mention that the formation of the silica layer not only prevents the leakage of the nanoparticles but also renders the hybrid material water dispersible, a key aspect for their use in biomedia. Since silica is a biocompatible and FDA (Food and Drug Administration) approved material, these novel Fe_3O_4@GNF@SiO_2 nanocapsules arise as a promising material for biotechnology research. In this paper, the MRI tests in the present work have already indicated good r_2^* relaxivities which is comparable with commercial MRI contrast agent, revealing the potential application in bio-imaging test. It is worth to believe that with the combination of biocompatible SiO_2 surface and good r_2^* relaxivities, this kind of nanocapsules may have promising application in magnetic therapy, magnetic manipulation, drug delivery and disease diagnose.

RSC Advances

PAPER

View Article Online
View Journal | View Issue

Cite this: *RSC Adv.*, 2017, **7**, 24690

Novel Fe_3O_4@GNF@SiO_2 nanocapsules fabricated through the combination of an *in situ* formation method and SiO_2 coating process for magnetic resonance imaging†

Changyong Lu,*[ab] Stefania Sandoval,[b] Teresa Puig,[b] Xavier Obradors,[b] Gerard Tobias,[b] Josep Ros[a] and Susagna Ricart[b]

Received 10th April 2017
Accepted 28th April 2017

DOI: 10.1039/c7ra04080f

rsc.li/rsc-advances

An *in situ* approach for the synthesis of Fe_3O_4 nanoparticles combined with a SiO_2 coating process was employed to prepare Fe_3O_4@GNF@SiO_2 nanocapsules. Graphitised nanofibres (GNF) were initially filled with iron(III) acetylacetonate, and used as a precursor for the synthesis of ultrasmall Fe_3O_4 nanoparticles (4.6 nm in diameter) inside the cavities of GNF (Fe_3O_4@GNF) with a high density. By using a silica coating process, Fe_3O_4@GNF@SiO_2 nanocapsules were obtained. The presence of the silica shell not only prevented leakage of the nanoparticles from inside the GNF but also protected the magnetite nanoparticles from dissolution, even in harsh acidic conditions. Furthermore, the silica coating resulted in an increased dispersability of the nanocomposites in water. Magnetic resonance imaging (MRI) studies indicate relatively high r_2^* relaxivities for Fe_3O_4@GNF nanocomposites and Fe_3O_4@GNF@SiO_2 nanocapsules revealing the potential application of these hybrid materials for bioimaging. Therefore, the coating of filled GNF with silica is as an excellent strategy for the protection of encapsulated payloads.

Introduction

With the increasing demand for new materials with special properties for our society, single-phase nanomaterials may not be capable of fulfilling all the requirements. Due to the excellent mechanical, electrical and optical properties of carbon nanostructures such as carbon nanotubes (CNTs)[1] and hollow graphitised nanofibres (GNF),[2] the formation of carbon nanohybrids has become an efficient way to combine the attractive properties of carbon nanostructures with those of other materials such as catalysts, magnetic nanoparticles, or photovoltaic materials.[3,4] The resulting hybrids not only benefit from the properties each constituent element but also from the synergistic effect that results in unique properties and superior performance.[5] The tubular nature of GNF and CNTs allows the formation of hybrids materials *via* modification of the external walls or by encapsulation of selected materials into their cavity. The first report about filling carbon nanostructure was a theoretical study by Pederson and Broughton who showed that fullerene tubules could draw molecules from liquid or vapor phase into their inner channels by capillary force.[6] After that, a wide variety of both organic and inorganic materials have been encapsulated or even grown inside carbon nanotubes and carbon nanofibers forming hybrid structures. For example, metal halides,[7] metallic nanowires,[8] low dimensional silica-based materials,[9] fluorescent polystyrene beads,[10] and individual layers of graphene[11] and related 2D materials[12] have all been encapsulated inside CNTs. Due to their small inner diameter, although single-walled carbon nanotubes and multi-walled carbon nanotubes have been filled with a variety of nanomaterials, the amount of material that can be encapsulated is limited. On another side, hollow graphitised nanofibres (GNF) would be promising for encapsulating nanomaterials because of the relative large inner diameter.[13] Andrei N. Khlobystov and his colleagues successfully synthesize Au nanoparticles inside GNF[14,15] and assemble Mn_3O_4 nanoparticles inside GNFs[16] making this kind of nanohybrids promising for the application in catalysis and spintronic devices. Pt and RuO_2 nanoparticles can be synthesized and filled inside the nanofiber showing potential applications in electrocatalysis, charge storage and fuel cell research.[17–19] Organic materials like fullerene-tagged [Cu-(salen)] catalysts and fullerene-free Pd(II) salen catalysts were immobilized inside GNF to form well-defined heterogeneous catalysts with excellent stability and recyclability.[20,21] Recently, researchers also found out that Pt

[a]Departament de Química, Edifici C Facultat de Ciències, Universitat Autònoma de Barcelona (UAB), Cerdanyola del Vallès, Barcelona 08193, Spain. E-mail: lu.changyong@e-campus.uab.cat

[b]Institute of Materials Science of Barcelona (ICMAB-CSIC), Campus de la UAB, Cerdanyola del Vallès, Barcelona 08193, Spain

† Electronic supplementary information (ESI) available: Detail of materials, instruments and experiments, electron diffraction pattern, thermal gravity cure, and inductively coupled plasma mass spectrometry study. See DOI: 10.1039/c7ra04080f

nanoparticles immobilized in shortened hollow graphitized carbon nanofibers could form an extremely stable electrocatalyst shown superior properties compared with commercial Pt/C electrocatalyst.[22] It is also worth to mention that GNF loaded with magnetic nanoparticles exhibit a large variety of current and potential applications in hyperthermia therapeutic and magnetic resonance imaging research.[23]

Several strategies have been employed to load the inner cavities of carbon nanotubes,[24] but regardless of the method employed, bulk filling typically results in samples that contain non-encapsulated material external to the walls. Strategies to remove this external material include the use of reverse micelles[25] and selective solvent mixtures,[26] leading to samples of open-ended filled tubes clean of external material. In order to provide protection of the encapsulated cargo several strategies have been explored to seal or cork the ends. The first report on the formation of permanently sealed "carbon nanocapsules" (filled carbon nanotubes with closed ends) involved high thermal annealing of single-walled carbon nanotubes, which results in the spontaneous end-closing forming covalent bonds.[27] Several other strategies have followed to block, at least partially, the open ends of the CNTs and GNF, including the use of fullerenes,[28,29] gold,[30,31] silica,[32] and a mixture of metal oxide nanoparticles.[33] Removable corks have also been designed for the development of controlled release systems.[30,31,34] It is also possible to coat the whole surface of nanohybrids with an inert protective shell. Following the work by Rao *et al.*, where a protective layer of carbon was deposited on the surface of previously filled carbon nanotubes,[35] Hampel *et al.* have recently used this strategy to prevent the release of toxic gadolinium from CNTs.[36] The carbon layer has been deposited by thermal treatment of the filled CNTs using either acetylene or benzene vapor. While there are several papers about sealing the ends of CNTs, the work about closing the ends of GNF still remains challenging due to their large diameter; only a few reports talk about using graphene or metal particles to cork the ends of GNF.[37,38]

Among the different applications of filled carbon nanostructures, their use in the biomedical field for both imaging and therapy is taking the lead.[39] In this area, the encapsulation of magnetic materials is of interest for the development of contrast agents for magnetic resonance imaging (MRI) and as therapeutic materials by hyperthermia.[23] By capillary action, GNF and CNTs can be loaded with pre-formed magnetic iron oxide nanoparticles.[40–42] It is also possible to use GNF and CNTs as templates for the *in situ* synthesis of iron oxide nanoparticles in their interior.[33,43,44] Despite several authors have reported on the magnetic properties of the resulting hybrids, their performance as MRI test has been barely investigated.[33]

Here we combined the *in situ* synthesis of Fe_3O_4 nanoparticles inside the cavities of GNF and the SiO_2 coating process to fabricate novel Fe_3O_4@GNF@SiO_2 nanocapsules. The hybrid materials present a complete filling of the inner GNF cavities with magnetite nanoparticles, which in turn are sealed with a protective SiO_2 coating. Due to the presence of the silica layer, the obtained nanocapsules still present a good magnetic response even after an acid treatment. It is also worth to mention that the formation of the silica layer not only prevents the leakage of the nanoparticles but also renders the hybrid material water dispersible, a key aspect for their use in biomedia. Since silica is a biocompatible and FDA approved material, these novel Fe_3O_4@GNF@SiO_2 nanocapsules arise as a promising material for biotechnology research. So far, the MRI tests in the present work have already indicated good r_2^* relaxivities revealing the potential application in bio-imaging test. It is worth to mention here that with the combination of biocompatible SiO_2 surface and good r_2^* relaxivities, this kind of nanocapsules may have promising application in magnetic therapy, magnetic manipulation, drug delivery and disease diagnose.

Results and discussion

Functional GNF with magnetic nanoparticles could combine the features of magnetic nanoparticles and GNF, resulting in novel physical and chemical properties. The role of different experimental conditions on the *in situ* synthesis of magnetic nanoparticles was initially assessed. Two samples of acid treated GNF were impregnated with the iron precursor, and independently submitted to thermal activation by either traditional heating with a heating plate or *via* a controlled microwave irradiation process. Both protocols lead to the formation of iron oxide nanoparticles inside GNF (Fig. 1).

Detailed analysis by transmission electron microscopy (TEM) of the sample prepared by traditional thermal activation at 200 °C (Fig. 1a and b), reveals the complete filling of the inner cavities of the GNF with very small nanoparticles (pristine GNF in Fig. S1†). The presence of some nanoparticles decorating the external walls is also visible. A high-resolution image is presented in the Fig. 1b to better appreciate the size of the nanoparticles, which have an average diameter of 4.6 ± 0.5 nm. When the Fe_3O_4 nanoparticles are synthesized in benzyl alcohol without presence of GNF, larger (7–8 nm) nanoparticles are formed,[45] indicating the role of the GNF as templates during the *in situ* growth. It is worth to mention that, the amount of $Fe(acac)_3$ used in the synthesis of Fe_3O_4@GNF nanocomposites is very important to make the GNF fully filled with nanoparticles. For instance, when the concentration of initial reactant $Fe(acac)_3$ is reduced from 1 to 0.1 mmol, the obtained GNF presented lower density of nanoparticles inside (see Fig. S3†).

Since magnetic nanoparticles can be prepared by microwave treatment and GNF are highly microwave absorbing materials, the synthesis of the nanoparticles was next done under microwave irradiation. This allows us to compare the effect of microwave irradiation on the formation of the hybrids. TEM analysis also confirms the presence of iron oxide nanoparticles inside the cavities of the GNF (Fig. S4†). It is noteworthy that a partial filling of the nanotubes is observed, with a bubble-type morphology, which might come from the rapid heating process by microwave irradiation.

Finally, the effect of surface functionalization of GNF on the *in situ* formation of metal oxide nanoparticles was investigated. Steam cleaned GNF were used to prepare iron oxide nanoparticles inside the cavities by traditional thermal activation.

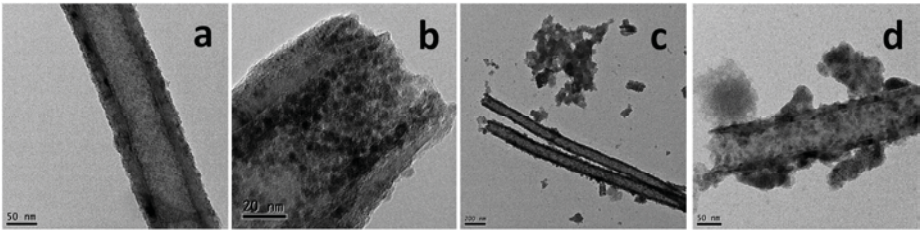

Fig. 1 (a) TEM image of Fe_3O_4@GNF nanocomposites prepared using acid treated GNF by traditional thermal activation, (b) high magnification image of Fe_3O_4@GNF nanocomposites prepared using acid treated GNF; (c and d) Fe_3O_4@GNF nanocomposites prepared using surface clean GNF (without nitric acid treatment) by traditional thermal activation.

TEM analysis (Fig. 1c and d) indicates the presence of iron oxide nanoparticles, but the loading density is not as high as when using acid treated GNF (Fig. 1a and b). This could be explained by the low dispersibility of the steam cleaned GNF in ethanol which might hinder their complete filling with the iron precursor. Furthermore, aggregated nanoparticles are also observed in Fig. 1e and f which might account for the decomposition of the non-encapsulated $Fe(acac)_3$ precursor still remaining outside the steam cleaned GNF, although leakage of nanoparticles during the washing process cannot be disregarded. Therefore, a preliminary conclusion can be made according to the discussion above based on TEM analysis: iron oxide filled GNF can be synthesized with a high filling density by using acid treated GNF and traditional thermal activation. Thus, this sample was employed for all the studies presented from now on. Finally, it is worth to mention that, although Fe_3O_4@GNF nanocomposites are prepared with lower loading density *via* microwave irradiation than with the thermal approach, further investigation is needed since it is possible to explore more in the relation with the confinement effect and high microwave effect coming from the carbon structure.

X-ray diffraction (XRD) analysis was next performed on the sample of filled tubes to determine the nature and structure of the synthesized nanoparticles. The most intense peaks observed in the XRD pattern in Fig. 2 could be assigned to carbon (JCPDS no. 41-1487) and to the presence of either magnetite (JCPDS no. 19-0629) or maghemite (JCPDS no. 39-1346). The existence of iron(II) oxide (JCPDS no. 89-7100) is also detected. According to our previous studies on the synthesis of magnetic nanoparticles in the absence of GNF, the employed protocol should lead to the formation of magnetite nanoparticles (Fe_3O_4).[45] The presence of small nanoparticles is responsible for the relatively low signal to noise ratio in the XRD pattern. No peaks of iron(III) acetylacetonate which was used as the reactant are observed suggesting a complete decomposition by the thermal treatment. The wide peaks in the pattern can be attributed to the small size of the nanoparticles and may be explained by the confinement effect of GNF.

Magnetic measurements were carried out on the Fe_3O_4@GNF nanocomposites at 5 K (Fig. 3). The magnetization saturation value steadily increases as a function of the applied magnetic field indicating that the nanoparticles in the GNF are magnetically active, reaching a saturation magnetization of 34.5 emu g^{-1}. The curve also displays a very small hysteresis featured by coercive field (H_c) of 280 Oe indicating a ferrimagnetic behavior. The magnetic behavior of the Fe_3O_4@GNF

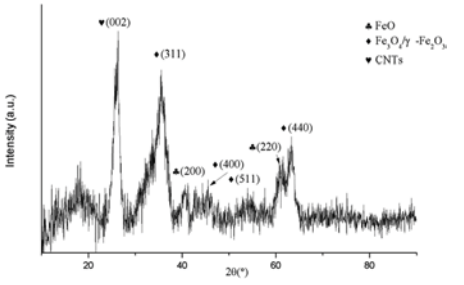

Fig. 2 X-ray diffraction pattern of Fe_3O_4@GNF nanocomposites prepared using acid treated GNF by traditional thermal activation.

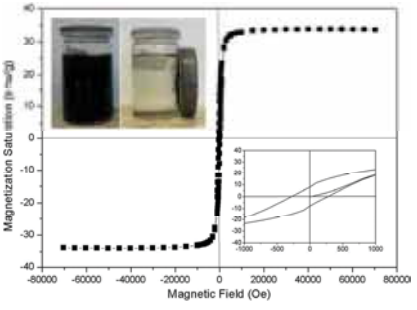

Fig. 3 Hysteresis loops at 5 K of Fe_3O_4@GNF nanocomposites prepared using acid treated GNF by traditional thermal activation. Inset top-left: photos of the nanocomposites dispersed in ethanol before and after (10 min) contact with an external magnet. Inset bottom-right: detail of magnetization at the low magnetic field region.

composites can be already appreciated by placing a magnet close to a dispersion of the nanocomposite in ethanol (see inset in Fig. 3). The image demonstrates that the nanocomposite can be easily manipulated by an external magnet as all the nanocomposite was separated from the solution within just few seconds. The fact that the hybrids can be easily separated in this manner is a clear advantage for their manipulation when compared to conventional filtration or centrifugation processes.

The amount of nanoparticles present in the nanocomposite was quantified by thermogravimetric analysis (TGA) under oxygen (Fig. S2†). The residue obtained after the complete combustion of the GNF at 600 °C corresponds to the Fe_3O_4 nanoparticles present in the sample which get oxidized to Fe_2O_3 during the TGA analysis. The amount of magnetite nanoparticles was calculated to 39.9 wt% based on the assumption that all the nanoparticles are magnetite. The theoretical value of the saturation magnetization, assuming that all the nanoparticles are pure Fe_3O_4 and taking into account that bulk Fe_3O_4 has a saturation magnetization of 92 emu g^{-1} is about 36.7 emu g^{-1} which was slightly larger than the magnetization saturation data and can account for the presence of a small amount of FeO or be due to the fact that the magnetization saturation values of nanoparticles is usually smaller than that of the bulk.[46]

To complete the characterization of the nanocomposites, scanning transmission electron microscopy (STEM) and energy electron loss spectroscopy (EELS) were employed to determine the distribution of the Fe_3O_4 nanoparticles in the nanocomposite. Both STEM and EELS in Fig. 4 confirms the presence of a large amount of nanoparticles filling the inner cavities of the nanotubes. A small fraction of magnetite nanoparticles is also visible outside the GNF which correspond to the iron signals around 30 nm and 100 nm.

The stability of the hybrid materials was next assessed by washing the as-synthesized Fe_3O_4@GNF nanocomposites (Fig. 5a) with different washing times using the procedure described in the Experiment part. Whereas an initial washing of the sample does not seem to release the encapsulated nanoparticles (Fig. 5b), when the samples were washed 2 times or more, leakage of the nanoparticles from the cavity was observed (Fig. 5c and d). As shown in the TEM images, the released nanoparticles tend to form big aggregates outside the GNF. The leakage of the magnetite nanoparticles hinders the application of the developed hybrids as contrast agents in the biomedical field since it would result in a misleading interpretation on the localization of the hybrid by *in vivo* imaging. To overcome this limitation, we propose a sealing strategy to shield materials inside GNF that consists on the formation of nanocapsules by

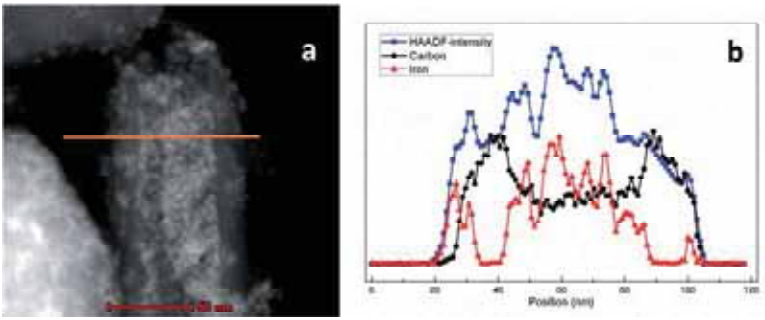

Fig. 4 (a) STEM and (b) high-angle annular dark-field imaging (HAADF), EELS analysis of Fe_3O_4@GNF nanocomposites prepared using acid treated CNTs by traditional thermal activation.

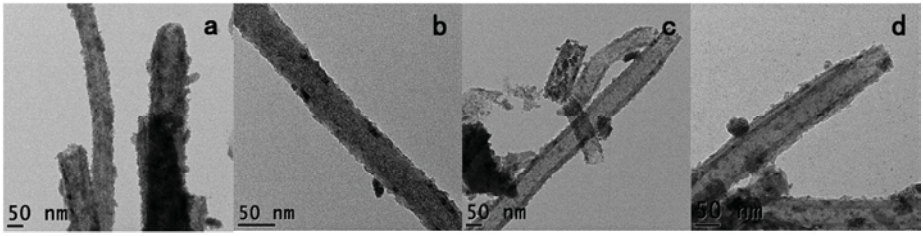

Fig. 5 TEM images of Fe_3O_4@CNF samples prepared using acid treated CNF by traditional thermal activation after different times of washing, (a) without wash, (b) 1 time, (c) 2 times and (d) 3 times.

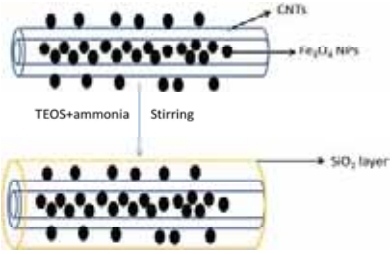

Scheme 1 Illustration of the formation of silica nanocapsules. Schematic representation of SiO_2 coating of Fe_3O_4@GNF nanocomposites.

silica coating the entire surface of GNF. In the Scheme 1 it is shown a representation of the proposed approach.

The surface of the filled GNF was coated with a SiO_2 shell *via* a straightforward method. The synthesized Fe_3O_4@GNF nanocomposites were simply mixed with TEOS (tetraethyl orthosilicate) in basic conditions which lead to a hydrolysis reaction. The FT-IR (Fig. 6) spectrum of the Fe_3O_4@GNF@SiO_2 nanocapsules shows absorption peaks at 795 cm^{-1}, 942 cm^{-1}, 1048 cm^{-1}, 1150 cm^{-1} and 1205 cm^{-1} attributed to the formation of the SiO_2 layer[47] on the surface of Fe_3O_4@GNF composites. A HR-TEM image of the prepared Fe_3O_4@GNF@SiO_2 nanocapsules is presented in Fig. 8a. In order to test the sealing capabilities of the developed SiO_2-based nanocapsules, the Fe_3O_4@GNF@SiO_2 were washed with an excessive amount of an aqueous solution of HCl. It is noteworthy that the cavities of the tubes were still fully filled with Fe_3O_4 nanoparticles (Fig. 7b and c), providing direct evidence that the SiO_2 coating is an efficient way to prevent the dissolution and leakage of the encapsulated compounds.

The magnetic behavior of Fe_3O_4@GNF@SiO_2 nanocapsules was also confirmed by applying an external magnet to a dispersion of the sample. As it can be seen in Fig. 8b, the acid washed Fe_3O_4@GNF@SiO_2 nanocapsules can be easily separated by the external magnetic field. It is worth to mention that the SiO_2 shell not only confers robustness to the prepared hybrid but also enhances its dispersity. Although the Fe_3O_4@GNF nanocomposites can also be separated with the external magnet (Fig. 8a), some precipitation is observed on the bottom of the vial which was also visible in the inset image of Fig. 3 indicates the relatively low dispersion in polar solvents. This simple analysis already suggests that the coating of SiO_2 improves the dispersion of the developed nanocomposites which is crucial for their application in biomedia.

The formation of the Fe_3O_4@GNF@SiO_2 nanocapsules (acid washed) was further confirmed by an EDS line profile

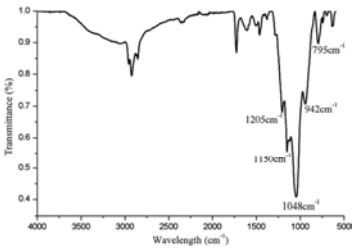

Fig. 6 FT-IR spectra curve of Fe_3O_4@GNF@SiO_2 nanocomposites.

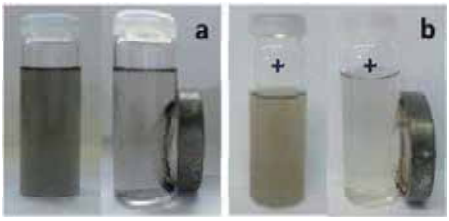

Fig. 8 Photos of (a) Fe_3O_4@GNF nanocomposites and (b) Fe_3O_4@-CNF@SiO_2 nanocapsules (after being washed with an HCl aqueous solution), before and after (10 min) applied external magnet. The same iron concentration was employed for the samples, which were dispersed in ethanol.

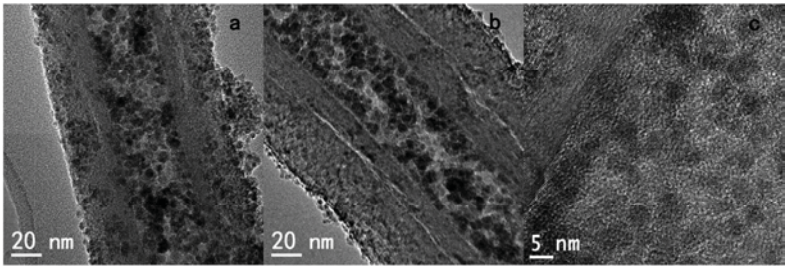

Fig. 7 HR-TEM images of Fe_3O_4@GNF@SiO_2 nanocapsules (a) before and (b) after washing with an HCl aqueous solution; (c) high magnification image of Fe_3O_4@GNF@SiO_2 nanocapsules after being washed with an HCl aqueous solution.

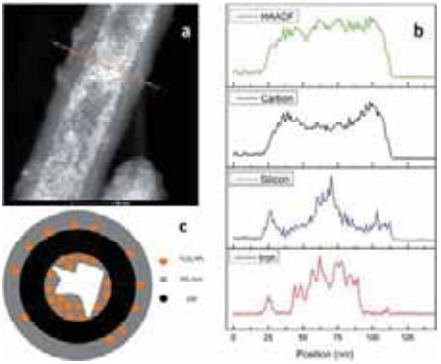

Fig. 9 (a) STEM and (b) EDS line profile analysis of the middle part of Fe_3O_4@GNF@SiO_2 nanocapsule after being washed by an HCl aqueous solution. (c) Schematic model of the Fe_3O_4@GNF@SiO_2 nanocapsules.

(Fig. 9a and b). First of all, a high Fe atomic ratio was observed inside the GNF confirmed the presence of Fe_3O_4 nanoparticles after the acid washing treatment suggesting the formation of protecting layer. As expected, Si signal could be observed on the external walls of the GNF, indicating the presence of the SiO_2 shell and the shell thickness is around 20 nm identified by the TEM studies (Fig. 8a and b). At the same time a high Si atomic ratio is visible in the same position where the atomic content of iron is also high (especially inside the GNF) which suggests that the SiO_2 was formed on the surface of the Fe_3O_4 nanoparticles. It is also observed that the GNF are not fully filled with nanoparticles, indicating a partial leakage of Fe_3O_4 nanoparticles during the hydrolysis of TEOS. A schematic model of the developed nanocapsules is presented in Fig. 9c, suggesting that the SiO_2 layer was not only formed on the external surface of the GNF but also inside the cavity. ICP-MS analysis of the Fe_3O_4@GNF@SiO_2 nanocapsules (Table S1†) after the complete digestion of the sample reveals the presence of 6.75 wt% of magnetite nanoparticles and a 65 wt% of silica coating. The relative fraction of GNF would then be 28.25 wt%. In agreement with TEM analysis, ICP-MS confirms the partial leakage of magnetite nanoparticles during the hydrolysis of TEOS. TGA analysis of the Fe_3O_4@GNF@SiO_2 nanocapsules (Fig. S5†) reveals a solid residue of *ca.* 85 wt% (at 900 °C). The TGA residue should correspond to Fe_2O_3 (from Fe_3O_4) and the silica coating, since the complete combustion of the GNF would be expected at this temperature. The high solid residue collected after the TGA indicates that some GNF could be protected by the silica coating from oxidation during the TGA.

Since magnetic nanocomposites show great potential as MRI contrast agents,[48,49] relaxivity measurements of Fe_3O_4@GNF nanocomposites and Fe_3O_4@GNF@SiO_2 nanocomposites were performed to evaluate their potential application as MRI contrast agents. The transverse R_2^* relaxation rates of Fe_3O_4@GNF nanocomposites and Fe_3O_4@GNF@SiO_2 nanocomposites dispersed in 1.5% agar and 1% Pluronic F127 solution at various Fe concentration were measured at 7 T. Fig. 10 shows the phantom MR imaging of the samples. The relaxation times of these two nanocomposites were plotted *versus* the iron concentration, revealing their potential as negative contrast agents. The r_2^* relaxivity of Fe_3O_4@GNF nanocomposites was calculated as 230.8 s^{-1} mM^{-1} which is 70% of the value of commercial Endorem contrast agent (325 s^{-1} mM^{-1}). The high viscosity of the agar solution makes the test media difficult to go inside the GNF, which can actually result in the determination of lower r_2^*. An increase on the r_2^* relaxivity to 252 s^{-1} mM^{-1} was observed for the sample coated with silica (Fe_3O_4@GNF@SiO_2) making it an appealing probe for MRI test. In the meantime, the biocompatible SiO_2 surface of these nanocapsules will make them more dispersible in bio-media and easy to be functionalized with biomolecules and other drugs indicating the promising application as a multifunctional tools in biomedicine research.

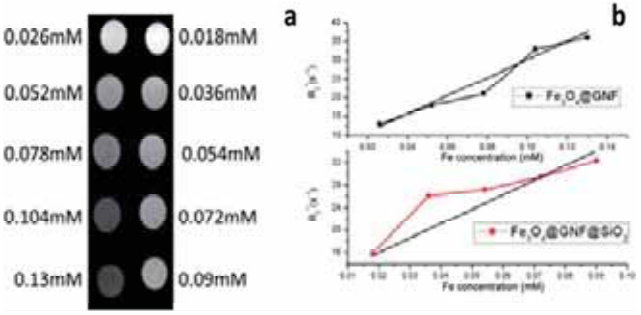

Fig. 10 (a) Phantom MR imaging of Fe_3O_4@GNF nanocomposites (left) and Fe_3O_4@GNF@SiO_2 nanocapsules (right), (b) R_2^* relaxation time analysis as a function of Fe concentration.

Conclusions

In the present study, we have developed *in situ* synthesis of ultra-small iron oxide nanoparticles (4.6 ± 0.5 nm) inside the cavities of GNF with a high filling density (39.9 wt% of Fe_3O_4). The magnetic properties of the prepared nanocomposites allow an easy manipulation and separation of the sample with an external magnet. Furthermore, we reported on the use of silica as a sealing agent to obtain novel Fe_3O_4@GNF@SiO_2 nanocapsules. The completely sealed SiO_2 layer prevented leakage of the nanoparticles and protected them from dissolution in harsh conditions (HCl). The developed silica nanocapsule not only offers protection of the encapsulated payload but also increases the dispersability of the hybrids, a key advantage for their application in the biomedical field. MRI studies of these two nanocomposites, namely Fe_3O_4@GNF and Fe_3O_4@GNF@SiO_2, confirm their potential as negative contrast agents. Therefore, the prepared Fe_3O_4@GNF@SiO_2 nanocapsules combine excellent properties for their use as biomedical probes, including robustness, dispersability and contrast enhancement. We believe that the silica coating strategy presented herein for the containment of iron oxide nanoparticles inside GNF will also allow protection of other confined materials and decoration of biomolecules. In summary, the magnetic Fe_3O_4@GNF@SiO_2 nanocomposites with biocompatible surface would have potential application as a multifunctional tool in biomedicine research and their applications in other fields are still need further study.

Acknowledgements

We acknowledge financial support from Spanish Ministry of Economy and Competitiveness through the "Severo Ochoa" Programme for Centres of Excellence in R&D (SEV-2015-0496), CONSOLIDER Excellence Network (MAT2015-68994-REDC), COACHSUPENERGY project (MAT2014-51778-C2-1-R, co-financed by the European Regional Development Fund) and CHALENG (MAT2014-53500-R). We also thank support from the European Union for EUROTAPES project (FP7-NMP-Large-2011-280432) and from the Catalan Government with 2014-SGR-753 and Xarmae. We also acknowledge financial support through PIE 201660E013 (CSIC) and Chinese Scholarship Council (CSC).

Notes and references

1 S. Iijima, *nature*, 1991, **354**, 56–58.
2 Y. Chen, X. Li, K. Park, J. Song, J. Hong, L. Zhou, Y.-W. Mai, H. Huang and J. B. Goodenough, *J. Am. Chem. Soc.*, 2013, **135**, 16280–16283.
3 D. Eder, *Chem. Rev.*, 2010, **110**, 1348–1385.
4 B. K. Balan and S. Kurungot, *Inorg. Chem.*, 2012, **51**, 9766–9774.
5 C. J. Shearer, A. Cherevan and D. Eder, *Adv. Mater.*, 2014, **26**, 2295–2318.
6 M. R. Pederson and J. Q. Broughton, *Phys. Rev. Lett.*, 1992, **69**, 2689.
7 J. Sloan, A. I. Kirkland, J. L. Hutchison and M. L. H. Green, *Chem. Commun.*, 2002, 1319–1332, DOI: 10.1039/b200537a.
8 L. Guan, K. Suenaga, S. Okubo, T. Okazaki and S. Iijima, *J. Am. Chem. Soc.*, 2008, **130**, 2162–2163.
9 Z. Liu, S.-K. Joung, T. Okazaki, K. Suenaga, Y. Hagiwara, T. Ohsuna, K. Kuroda and S. Iijima, *ACS Nano*, 2009, **3**, 1160–1166.
10 B. M. Kim, S. Qian and H. H. Bau, *Nano Lett.*, 2005, **5**, 873–878.
11 A. Chuvilin, E. Bichoutskaia, M. C. Gimenez-Lopez, T. W. Chamberlain, G. A. Rance, N. Kuganathan, J. Biskupek, U. Kaiser and A. N. Khlobystov, *Nat. Mater.*, 2011, **10**, 687–692.
12 L. Cabana, B. Ballesteros, E. Batista, C. Magén, R. Arenal, J. Oró-Solé, R. Rurali and G. Tobias, *Adv. Mater.*, 2014, **26**, 2016–2021.
13 E. Castillejos, P.-J. Debouttière, L. Roiban, A. Solhy, V. Martinez, Y. Kihn, O. Ersen, K. Philippot, B. Chaudret and P. Serp, *Angew. Chem.*, 2009, **121**, 2567–2571.
14 A. La Torre, M. d. C. Giménez-López, M. W. Fay, G. A. Rance, W. A. Solomonsz, T. W. Chamberlain, P. D. Brown and A. N. Khlobystov, *ACS Nano*, 2012, **6**, 2000–2007.
15 A. La Torre, G. A. Rance, J. El Harfi, J. Li, D. J. Irvine, P. D. Brown and A. N. Khlobystov, *Nanoscale*, 2010, **2**, 1006–1010.
16 M. d. C. Gimenez-Lopez, A. La Torre, M. W. Fay, P. D. Brown and A. N. Khlobystov, *Angew. Chem., Int. Ed.*, 2013, **52**, 2051–2054.
17 B. K. Balan, S. M. Unni and S. Kurungot, *J. Phys. Chem. C*, 2009, **113**, 17572–17578.
18 B. Cornelio, A. R. Saunders, W. A. Solomonsz, M. Laronze-Cochard, A. Fontana, J. Sapi, A. N. Khlobystov and G. A. Rance, *J. Mater. Chem. A*, 2015, **3**, 3918–3927.
19 R. Vellacheri, V. K. Pillai and S. Kurungot, *Nanoscale*, 2012, **4**, 890–896.
20 M. A. Lebedeva, T. W. Chamberlain, M. Schröder and A. N. Khlobystov, *Chem. Mater.*, 2014, **26**, 6461–6466.
21 M. A. Lebedeva, T. W. Chamberlain, A. Thomas, B. E. Thomas, C. T. Stoppiello, E. Volkova, M. Suyetin and A. N. Khlobystov, *Nanoscale*, 2016, **8**, 11727–11737.
22 M. del Carmen Gimenez-Lopez, A. Kurtoglu, D. A. Walsh and A. N. Khlobystov, *Adv. Mater.*, 2016, **28**, 9103–9108.
23 A. Stopin, F. Pineux, R. Marega and D. Bonifazi, *Chem.–Eur. J.*, 2015, **21**, 9288–9301.
24 M. Monthioux and E. Flahaut, *Mater. Sci. Eng., C*, 2007, **27**, 1096–1101.
25 J. Cook, J. Sloan, R. J. R. Heesom, J. Hammer and M. L. H. Green, *Chem. Commun.*, 1996, 2673–2674, DOI: 10.1039/cc9960002673.
26 Q. Fu, W. Gisela and D.-s. Su, *New Carbon Mater.*, 2008, **23**, 17–20.
27 L. Shao, G. Tobias, Y. Huh and M. L. H. Green, *Carbon*, 2006, **44**, 2855–2858.
28 L. Shao, T.-W. Lin, G. Tobias and M. L. H. Green, *Chem. Commun.*, 2008, 2164–2166, DOI: 10.1039/b800881g.
29 Y. Ren and G. Pastorin, *Adv. Mater.*, 2008, **20**, 2031–2036.

30 J. Li, S. Q. Yap, S. L. Yoong, T. R. Nayak, G. W. Chandra, W. H. Ang, T. Panczyk, S. Ramaprabhu, S. K. Vashist, F.-S. Sheu, A. Tan and G. Pastorin, *Carbon*, 2012, **50**, 1625–1634.

31 J. Li, S. L. Yoong, W. J. Goh, B. Czarny, Z. Yang, K. Poddar, M. M. Dykas, A. Patra, T. Venkatesan, T. Panczyk, C. Lee and G. Pastorin, *Int. J. Nanomed.*, 2015, **10**, 7425–7744.

32 X. Chen, H. Chen, C. Tripisciano, A. Jedrzejewska, M. H. Rümmeli, R. Klingeler, R. J. Kalenczuk, P. K. Chu and E. Borowiak-Palen, *Chem.–Eur. J.*, 2011, **17**, 4454–4459.

33 X. Liu, I. Marangon, G. Melinte, C. Wilhelm, C. c. Ménard-Moyon, B. P. Pichon, O. Ersen, K. Aubertin, W. Baaziz and C. Pham-Huu, *ACS Nano*, 2014, **8**, 11290–11304.

34 P. Luksirikul, B. Ballesteros, G. Tobias, M. G. Moloney and M. L. Green, *Carbon*, 2010, **48**, 1912–1917.

35 B. C. Satishkumar, A. Govindaraj, J. Mofokeng, G. N. Subbanna and C. N. R. Rao, *J. Phys. B: At., Mol. Opt. Phys.*, 1996, **29**, 4925.

36 E. Fidiani, P. M. F. J. Costa, A. U. B. Wolter, D. Maier, B. Buechner and S. Hampel, *J. Phys. Chem. C*, 2013, **117**, 16725–16733.

37 J. Shin, K. Park, W.-H. Ryu, J.-W. Jung and I.-D. Kim, *Nanoscale*, 2014, **6**, 12718–12726.

38 Y. Shen, L. Li, K. Xiao and J. Xi, *ACS Sustainable Chem. Eng.*, 2016, **4**, 2351–2358.

39 M. Martincic and G. Tobias, *Expert Opin. Drug Delivery*, 2015, **12**, 563–581.

40 G. Korneva, H. Ye, Y. Gogotsi, D. Halverson, G. Friedman, J.-C. Bradley and K. G. Kornev, *Nano Lett.*, 2005, **5**, 879–884.

41 S. Kopyl, V. Bystrov, I. Bdikin, M. Maiorov and A. C. Sousa, *J. Mater. Chem. C*, 2013, **1**, 2860–2866.

42 S. Kopyl, A. Timopheev, V. Bystrov, I. Bdikin, B. Teixeira, E. Maevskij, N. Sobolev and A. Sousa, *J. Magn. Magn. Mater.*, 2014, **358**, 44–49.

43 W. Baaziz, X. Liu, I. Florea, S. Begin-Colin, B. P. Pichon, C. Ulhaq, O. Ersen, M. Soria-Sánchez, S. Zafeiratos and I. Janowska, *J. Mater. Chem. A*, 2013, **1**, 13853–13861.

44 W. Chen, X. Pan and X. Bao, *J. Am. Chem. Soc.*, 2007, **129**, 7421–7426.

45 E. Solano, L. Perez-Mirabet, F. Martinez-Julian, R. Guzmán, J. Arbiol, T. Puig, X. Obradors, R. Yañez, A. Pomar and S. Ricart, *J. Nanopart. Res.*, 2012, **14**, 1–15.

46 B. Xavier and L. Amílcar, *J. Phys. D: Appl. Phys.*, 2002, **35**, R15.

47 C. Lu, T. Puig, X. Obradors, S. Ricart and J. Ros, *RSC Adv.*, 2016, **6**, 88762–88769.

48 Q. L. Vuong, J. F. Berret, J. Fresnais, Y. Gossuin and O. Sandre, *Adv. Healthcare Mater.*, 2012, **1**, 502–512.

49 L. Sandiford, A. Phinikaridou, A. Protti, L. K. Meszaros, X. Cui, Y. Yan, G. Frodsham, P. A. Williamson, N. Gaddum and R. M. Botnar, *ACS Nano*, 2012, **7**, 500–512.

Support Information

Novel Fe_3O_4@GNF@SiO_2 nanocapsules fabricated through the combination of in-situ formation method and SiO_2 coating process for magnetic resonance imaging

Changyong Lu, [a,b] Stefania Sandoval, [b] Teresa Puig,[b] Xavier Obradors,[b] Gerard Tobias,[b] Josep Ros[a] and Susagna Ricart*[b]

Journal: RSC Advances

Corresponding Authors: Changyong Lu

Other Authors: Changyong Lu, [a,b] Stefania Sandoval, [b] Teresa Puig,[b] Xavier. Obradors,[b] Josep Ros,[a] and Gerard Tobias[b]

Address:

a. Departament de Quimica, Edifici C Facultat de Ciències, Universitat Autónoma de Barcelona（UAB）, Cerdanyola del Vallès, Barcelona 08193, Spain. E-mail: lu.changyong@e-campus.uab.cat

b. Institute of Materials Science of Barcelona (ICMAB-CSIC), Campus de la UAB, Cerdanyola del Vallès, Barcelona 08193, Spain. E-mail: ricart@icmab.es

Experimental procedure

2.1 Materials

Iron(III) acetylacetonate (99.9%), Benzyl alcohol (99%), Benzyl ether (98%), Ammonium hydroxide solution (30-33% NH_3 in H_2O) and Tetraethyl orthosilicate (TEOS) (98%) were used as received from Sigma-Aldrich (Madrid Spain). Ethanol (absolute PA 99.5%) was used as received from PanReac AppliChem (Barcelona Spain). GNF were supplied by Pyrograf (USA), the type is PR-24-XT-LHT.

2.2 Steam cleaning process of GNF

GNF were initially purified following the standard steam cleaning process. As received GNF were placed into the center of a silica tube, which was then loaded into the alumina tube of a horizontal furnace. Steam was introduced by bubbling argon through hot water (98ºC). The whole system was initially purged by Ar for 2h to remove atmospheric air. Then the furnace was heated to 900ºC and held at this temperature for 1.5h. After the reaction, the furnace was cooled down to room temperature, and the resulting black solid was collected. Then, the GNF were dispersed in 100 mL of a 6 M hydrochloric acid solution and refluxed at 110ºC for 6h. Subsequently, the GNF sample was washed with water and filtered by using a polycarbonate membrane (0.2 μm pore size) until the pH=7. Finally, the sample were dried at 60ºC for 24 h. We will refer to this sample as “steam treated GNF”.

2.3 Acid treatment of GNF

In a typical process, 10 mg of steam cleaned GNF were dispersed in 10 mL HNO_3 with the aid of an ultrasonic bath for 2 h. The mixture was then transferred to a round bottom flask and refluxed at 140℃ for 16 h and then allowed to cool down to room temperature. The sample was washed with water and filtered by using Nylon membrane (200 □m pore size) until the pH=7. After that, the black solid was collected from the top of the membrane and dried at 60ºC for 24 h. We will refer to this sample as “acid treated GNF”.

2.4 Synthesis of Fe_3O_4@GNF nanocomposites

The acid treated GNF (1 mg) were dispersed in a solution (20 mL ethanol) containing the iron precursor (0.358 g $Fe(acac)_3$,1mmol) by ultrasonic treatment for 2 h, followed by magnetic stirring for 24 h. Afterwards, the mixture

was dried at 60ºC for 24 h (the solvent was totally evaporated), and the obtained solid was redispersed in 20mL of benzyl alcohol through ultrasonic treatment for 2 h, and stirred for 24 h. The solid was collected by centrifugation (10000 rpm, 30 min) and dispersed in 20 mL of benzyl ether. The Fe_3O_4 nanoparticles were prepared employing two different protocols. The first one involves traditional thermal annealing using a heating plate, where the iron precursor filled GNF are heated to 200ºC in benzyl ether in a round bottom flask at a heating rate of 1ºC/min and hold for 4 h under reflux. The second approach employs a microwave reactor with controlled atmosphere (Discover Explorer Hybrid from CEM Kamp-Lintfort Germany). The mixture is transferred into a microwave reaction vial where is rapidly heated to 200ºC and hold for 30min. In order to study the effect of the amount of $Fe(acac)_3$ on the final products, one mixture was prepared with only 0.0358g $Fe(acac)_3$ (0.1mmol) inside and the samples were synthesized via a traditional solvent thermal method.

In both synthesis, after the reaction the mixture was cooled to room temperature and washed. To do the washing process, 20 mL of ethanol were added to the mixture and an external magnet was applied to separate the solid, which was then redispersed in ethanol, and the process was repeated three times to get the Fe_3O_4@GNF. When necessary, the obtained samples were dispersed in ethanol for further characterization.

To shed some light on the role of the nitric acid treatment, an additional sample was prepared by applying the same experimental procedure, using a heating plate, on a sample of steam cleaned GNF.

2.5 Synthesis of Fe_3O_4@GNF@SiO_2 nanocapsules

The as synthesized Fe_3O_4@GNF hybrids were first dispersed in 10 mL of a ethanol/water mixture (v:v=10:1) containing 0.1 mL of ammonium hydroxide. Then 50 µL of TEOS (tetraethyl orthosilicate) was added into the solution which was kept stirring for 12 h. The products were isolated with the aid of an external magnet and washed several times with water and ethanol mixture (v_{water}:$v_{ethanol}$=1:1).

To confirm the sealing efficiency of the SiO_2 coating, a fraction of the sample was dispersed in an excess volume of HCl aqueous solution (pH = 2) and kept stirring for 2 h. The solid was collected by applying an external magnet and washed several times with water.

2.6 Characterization and Measurements

Fourier transform infrared spectroscopy (ATR-FT-IR) was performed on a Bruker Tensor 27 Fourier transform infrared spectrometer (Golden gate) in a range of 600-4000 cm^{-1}. All samples were measured as a solid powder at room temperature.

Transmission electron microscope (TEM) and high resolution transmission electron microscopy (HR-TEM) measurements were conducted on a JEOL 1210 TEM microscope operated at 130 kV and a JEM-2011 HR-TEM microscope at 200 kV. Electron energy loss spectroscopy (EELS) and Energy-dispersive X-ray spectroscopy (EDS) analysis (using High-angle annular dark-field imaging (HAADF)) were performed in a FEI Tecnai G2 F20 S-TWIN HR(S) TEM at 200 kV. For the analyses, one drop of the ethanol dispersion of the Fe_3O_4@GNF and the SiO_2 coated Fe_3O_4@GNF nanocomposites were independently deposited onto carbon-coated copper grids. In order to minimize the aggregation of the nanoparticles, the copper grids were laid on top of a filter paper during the drying process.

X-ray powder diffraction studies (XRD) were performed on D5000 Siemens X-Ray powder diffractometer in reflection mode using Cu Kα λ=1.5406 Å radiation in a range of $10° \leq 2\theta \leq 90°$.

Field-dependent magnetization curves were acquired by SQUID (Quantum design MPMS XL-7T) under a magnetic field from 0 to ±70000 Oe at 5K.

Thermogravimetric analyses (TGA) were carried out on a NETZSCH-STA 449 F1 Jupiter thermal analysis system from room temperature to 1000°C under an O_2 flow.

Inductively coupled plasma mass spectrometry (ICP-MS) tests were carried out on an Agilent 7500ce analysis system.

Phantom MR imaging were performed at 7 T horizontal MR scanner (Bruker Biospec 7T MRI). The concentrations of Fe in the different samples were calculated according to the results from TGA and ICP-MS. Fe_3O_4@GNF and Fe_3O_4@GNF@SiO_2 nanocomposites were dispersed in a solution of 2% Pluronic F-127 for 30 min using a bath sonicator (Nahita Model I 610/3). Dispersed nanocomposites were mixed with an equal volume of melted agar solution (3%, w/v in water at 90℃) to achieve final Fe concentrations of Fe_3O_4@GNF nanocomposites and Fe_3O_4@GNF@SiO_2 nanocomposites ranging from 0.026 mM to 0.13 mM and 0.018mM to 0.09mM respectively in 1.5% agar in water.

References:

Cabana, L.; Ke, X.; Kepić, D.; Oro-Solé, J.; Tobías-Rossell, E.; Van Tendeloo, G.; Tobias, G., The role of steam treatment on the structure, purity and length distribution of multi-walled carbon nanotubes. Carbon 2015, 93, 1059-1067.

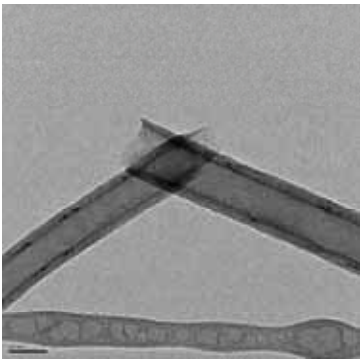

Figure S1. TEM image of the pristine CNF with open ends.

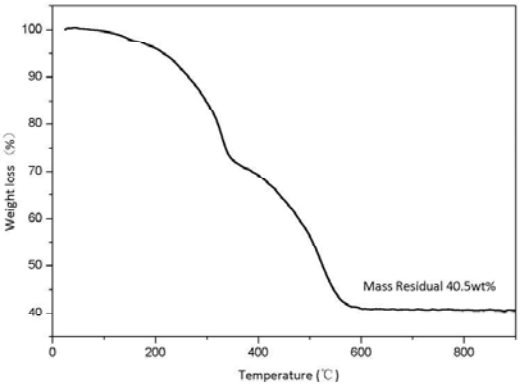

Figure S2. Thermogravimetric analysis under flowing oxygen of Fe_3O_4@GNF nanocomposites prepared using acid treated GNF by traditional thermal activation.

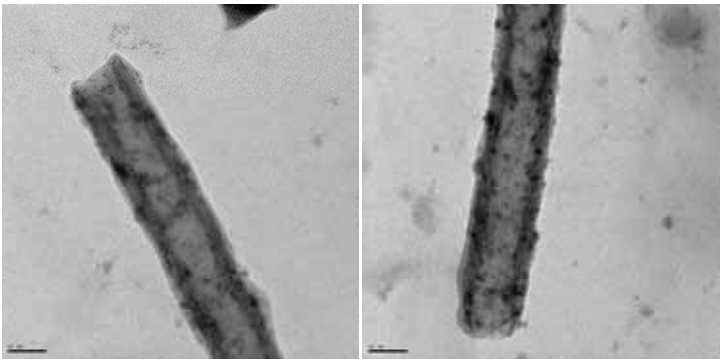

Figure S3. Fe_3O_4@GNF nanocomposites prepared using acid treated GNF, 0.0358g $Fe(acac)_3$ (0.1mmol) and standard thermal method.

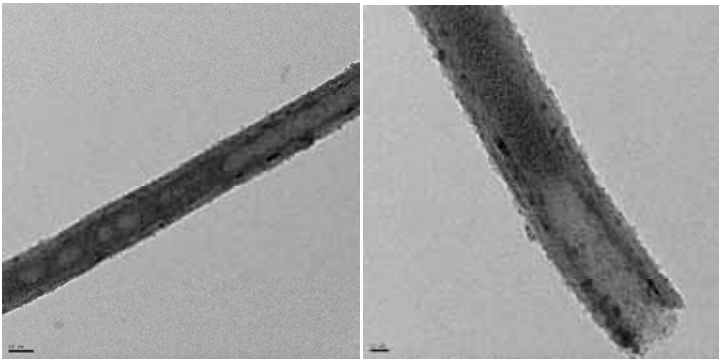

Figure S4. Fe_3O_4@GNF nanocomposites prepared using acid treated GNF under microwave irradiation

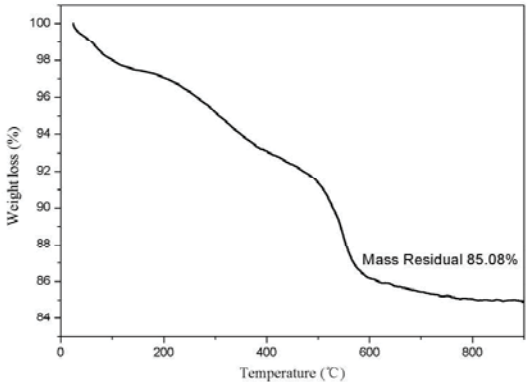

Figure S5. Thermogravimetric analysis of Fe_3O_4@GNF@SiO_2 nanocomposites under flowing oxygen.

Sample Name	Fe wt%	Si wt%
Fe_3O_4@GNF@SiO_2	4.9 %	19 %

Table S1. ICP-MS result of Fe_3O_4@GNF@SiO_2 nanocomposites

References

1. in *Metal Oxide Nanoparticles in Organic Solvents: Synthesis, Formation, Assembly and Application*, Springer London, London, 2009, pp. 1-5.
2. S. H. Joo, J. Y. Park, C.-K. Tsung, Y. Yamada, P. Yang and G. A. Somorjai, *Nat Mater*, 2009, **8**, 126-131.
3. A. V. Jovanovic, J. A. Flint, M. Varshney, T. E. Morey, D. M. Dennis and R. S. Duran, *Biomacromolecules*, 2006, **7**, 945-949.
4. G. Elmaci, C. E. Frey, P. Kurz and B. Zümreoğlu-Karan, *Inorganic Chemistry*, 2015, **54**, 2734-2741.
5. M. P. L. Werts, M. Badila, C. Brochon, A. Hébraud and G. Hadziioannou, *Chemistry of Materials*, 2008, **20**, 1292-1298.
6. B. T. Diroll and C. B. Murray, *ACS Nano*, 2014, **8**, 6466-6474.
7. J. Bang, J. Park, J. H. Lee, N. Won, J. Nam, J. Lim, B. Y. Chang, H. J. Lee, B. Chon, J. Shin, J. B. Park, J. H. Choi, K. Cho, S. M. Park, T. Joo and S. Kim, *Chemistry of Materials*, 2010, **22**, 233-240.
8. R. Ghosh Chaudhuri and S. Paria, *Chemical reviews*, 2011, **112**, 2373-2433.
9. R. Bardhan, S. Mukherjee, N. A. Mirin, S. D. Levit, P. Nordlander and N. J. Halas, *The Journal of Physical Chemistry C*, 2010, **114**, 7378-7383.
10. G. J. Leggett, *ACS Nano*, 2011, **5**, 1575-1579.
11. M. Nguyen, X. Sun, E. Lacaze, P. M. Winkler, A. Hohenau, J. R. Krenn, C. Bourdillon, A. Lamouri, J. Grand, G. Lévi, L. Boubekeur-Lecaque, C. Mangeney and N. Félidj, *ACS Photonics*, 2015, **2**, 1199-1208.
12. A. S. Urban, A. A. Lutich, F. D. Stefani and J. Feldmann, *Nano Letters*, 2010, **10**, 4794-4798.
13. C. L. Sajti, R. Sattari, B. N. Chichkov and S. Barcikowski, *The Journal of Physical Chemistry C*, 2010, **114**, 2421-2427.
14. A. Lehmuskero, P. Johansson, H. Rubinsztein-Dunlop, L. Tong and M. Käll, *ACS Nano*, 2015, **9**, 3453-3469.

15. W. J. Deng, W. Xia, C. Li and Y. Tang, *Journal of Materials Processing Technology*, 2009, **209**, 4521-4526.
16. A. C. Dodd, *Powder Technology*, 2009, **196**, 30-35.
17. R. Sasikumar and R. M. Arunachalam, *Materials Letters*, 2009, **63**, 2426-2428.
18. K. L. Sowers, B. Swartz and T. D. Krauss, *Chemistry of Materials*, 2013, **25**, 1351-1362.
19. A. M. Boies, S. Calder, P. Agarwal, P. Lei and S. L. Girshick, *The Journal of Physical Chemistry C*, 2012, **116**, 104-114.
20. J. D. Fowlkes, L. Kondic, J. Diez, Y. Wu and P. D. Rack, *Nano Letters*, 2011, **11**, 2478-2485.
21. M. Grzelczak, J. Vermant, E. M. Furst and L. M. Liz-Marzán, *ACS Nano*, 2010, **4**, 3591-3605.
22. D. W. Sinkovits and E. Luijten, *Nano Letters*, 2012, **12**, 1743-1748.
23. L. Jing, C. Yang, R. Qiao, M. Niu, M. Du, D. Wang and M. Gao, *Chemistry of Materials*, 2010, **22**, 420-427.
24. J. N. Solanki and Z. V. P. Murthy, *Industrial & Engineering Chemistry Research*, 2011, **50**, 12311-12323.
25. S. Mukhopadhyay, A. Yaghmur, M. Baidossi, B. Kundu and Y. Sasson, *Organic Process Research & Development*, 2003, **7**, 641-643.

Chapter 4 Other Applications about Fe_3O_4@SiO_2 Core-shell Nanoparticles

4.1 Cytotoxicity and MRI study of Fe_3O_4@SiO_2 core-shell nanoparticles

Due to the advantage of the combination of the special properties of core materials and shell materials nanoparticles with core-shell structure are promising candidates in the application in bio-medical research, for example in bio-imaging, drug delivery, hyperthermia therapy and disease diagnoses.

4.1.1 Introduction of core-shell nanoparticles application in bio-medical research

Until now, numerous research has been done on applying core-shell nanoparticles in biomedical research. For instance, Xiang Wu et al successfully synthesized a dye-Sensitized core/active Shell upconversion nanoparticles for optogenetics and bioimaging applications[1], Dae-Hwan Park et al. found out that the well-defined DNA core@metal hydroxide shell nanoparticles provide wide bioinspired applications range from diagnosing/tracing/collecting and sensing system via pre-functionalization of DNA with designed information[2], Ag nanoparticles covered with

mesoporous SiO_2 can be used as a nanocarriers for superior surface-enhanced Raman scattering imaging and pH trigged drug delivery in cancer therapy[3].

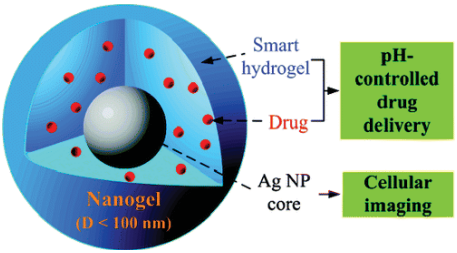

Figure 4.1 Illustration of smart Ag@Nanogels core–shell nanoparticles for cancer cell imaging and pH-regulated drug delivery[4]

4.1.2 Principle of magnetic resonance imaging

Magnetic resonance imaging (MRI) is a powerful bio-imaging technique for the diagnosis of disease of the tissue. As it is known to all, the majority of our body is water and atom nuclei with an odd number of nucleons (neutrons + protons) have net non-zero spin, caused by the rotation of charged nuclei, the MRI technique is the method to be use, taking advantage of the behaviour of H atoms in the water molecules of our body when applied external magnetic field.[5]

The H atoms in water molecules can be considered as charged spheres rotating with collinear angular momentum and a magnetic moment. In an MRI experiment, an external magnetic field is

first applied to the patient or tissue to make the spin of H atoms excited by the external magnetic field precess around that field. [6]The frequency of that precession is proportional to the external magnetic field and can be described by the Larmor equation[7]

$$\omega_0 = B_0 \times \gamma / 2\pi$$

ω_0 is Larmor frequency (in Hz), γ is a gyromagnetic ratio that depends on the nuclei and B_0 is the externally applied magnetic field (in tesla). Then when another oscillating electromagnetic field (a radio frequency (rf) pulsed field) perpendicular to the previous magnetic field is applied, the magnetic moments of H atoms will align in parallel with the rf field[8]. When the frequency of the rf field is the same as that of the previous external magnetic field, resonance phenomenon will occur, the hydrogen nuclei will absorb energy from the rf pulse[9]. The net magnetic vector comes to lie in the transverse plane, 90° to the direction of the previous external magnetic field. After that, the rf field is removed and the transverse magnetization of the H atom spin decreases along with the increasing of the longitudinal magnetization to its original strength[10], the transverse and longitudinal magnetic vector also changes. In a MRI instrument, a receiver coil is lain in the transverse plane, a voltage is generated in the receiver coil as a result of the changing of magnetic vector around the transverse plane during the procedure described above.[11] And this voltage can be used as the MRI signal to get phantom images and relaxation time values.[12]

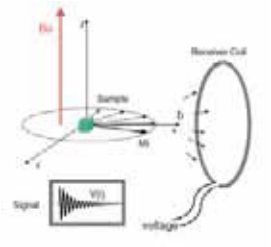

Figure 4.2 Schematic of how signal generated in a MRI system[9]

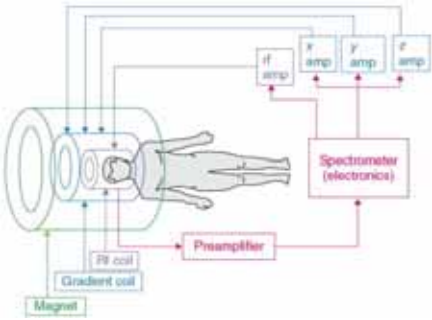

Figure 4.3 Schematic of major components of an MRI system[13]

The MRI signal intensity is expressed in gray levels: a high intensity signal appears in white and a weak intensity signal in black or dark gray. There are typically two kind of images signal consisted in MRI experiments, T_1-weighted(T_1W) and T_2-weighted (T_2W).

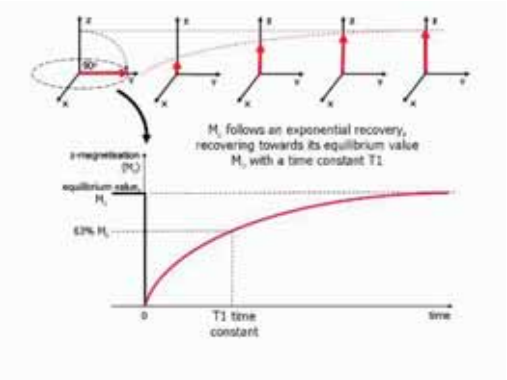

Figure 4.4 Schematic of T_1 relaxation process[14]

T_1-weighted: T_1 relaxation is the process by which the longitudinal magnetization is recovered (after the excitation pulse is applied) due to transfer of energy from the nuclear spin system to the neighbouring molecules (the lattice). It occurs in the z-direction (z-axis is often depicted as a vertical line). The T_1 relaxation time is a measure of the rate of transfer of energy from the nuclear spin system to the neighbouring molecules (the lattice). It is the time when 63% of the longitudinal magnetization has recovered.[8-10]

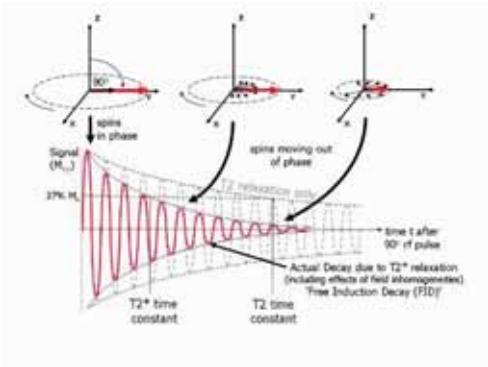

Figure 4.5 Schematic of transverse (T_2 and T_2^*) relaxation processes[14]

T_2-weighted: T_2 relaxation is the process by which the transverse magnetization decays due to dephasing of proton spins (spins becoming desynchronized). After the excitation pulse is applied, the magnetization flips 90 degrees from the longitudinal axis to the xy-plane. The transverse magnetization is initially maximum (due to coherent nuclear spins) but this arrangement is gradually lost due to field inhomogeneity and/or direct interactions between the spins (without energy transfer to the lattice). T_2 relaxation occurs on the xy-plane and is often depicted as the spreading of magnetic moments along the plane. The T_2 relaxation time is a measure of the rate of the decay of transverse magnetization within the xy-plane. It is the time when 63% of the transverse magnetization has decayed.[8, 10, 11, 15]

4.1.3 MRI contrast agents

The MRI contrast agents interact with H_2O protons and modify their relaxation times, or are

directly involved in the level of H_2O proton magnetization. Nowadays, there are many kinds of contrast agents, for example Gadolinium (Gd) complex agents for T_1 weighted imaging and iron oxide agents for T_2 weighted imaging.

Gadolinium (Gd) complex agents

Until now, the most widely used MRI contrast agents is based on the mechanism of longitudinal relaxation (T_1)[16]. When introducing molecules containing unpaired electrons (e^-) into the H_2O molecule environment, longitudinal relaxation process of the H_2O protons is much more effective, because the magnetic moment of the electron is 658 times stronger than that of the proton. Given its high electron spin (S=7/2) and slow electron spin relaxation, the trivalent Gd^{3+} ion is the most efficient relaxation agent among all paramagnetic cations. To avoid the toxicity of the free Gd^{3+} ion, it is functionalized with appropriate multidentate ligands. In this way, the gadolinium complexes will reduce the neighbour water hydrogens T_1 relaxation time. Since the formation of an MRI image requires the accumulation of many acquisitions to obtain a sufficient contrast, one can obtain more accumulations per unit time by simply reducing the time interval between two consecutive RF pulses (repetition time TR)[17]. Therefore the Gd^{3+} complex contrast agents in a particular location of a living tissue will result in a stronger positive enhancement signal[5, 7, 18].

Iron oxide agents

Another kind of contrast agents are iron oxide nanoparticles (Fe_3O_4 and γ-Fe_2O_3). They can be divided into two groups according to their size, SPIO (Super Paramagnetic Iron Oxides, average

diameter is larger than 50nm) and USPIO (Ultra-Small Super Paramagnetic Iron Oxides, average is smaller than 50nm). [5]The iron oxide nanoparticles can be considered as small magnets with good mobility. The existence of these nanoparticles can create strong inhomogeneity of magnetic field in the environment and therefore significantly reducing the T_2 relaxation time of H protons. Subsequently, a negative enhancement contrast can be obtained[19, 20].

In this chapter, the possibility of the use of the synthesized core-shell nanoparticles as contrast agents in MRI experiments is studied.

4.1.4 Synthetic process

4.1.4.1 Preparation of Fe_3O_4 nanoparticles and Fe_3O_4@SiO_2 core-shell nanoparticles

The Fe_3O_4 nanoparticles and Fe_3O_4@SiO_2 core–shell nanoparticles are prepared using the approaches described in the first paper[21] of Chapter 3. The Fe_3O_4@SiO_2 core–shell nanoparticles were dispersed in ethanol in concentration of 200mg/ml.

4.1.4.2 Cytotoxicity study of Fe_3O_4@SiO_2 core-shell nanoparticles with cells

Cell Culture maintenance. Human Epithelial Cervical Adenocarcinoma Cells were cultured

in complete medium: 1X Minimal Essential Medium (Gibco by Life Technologies) supplemented with 10% Fetal Bovine Serum (Biowest) and 2 mM L-Glutamine (Life Technologies). All cell lines were purchased from the ATCC and were maintained at 37ºC and humidified atmosphere of 5% CO_2 (standard conditions).

Fe_3O_4@SiO_2 NPs-cells association through scanning electron microscopy (SEM). Cells were seeded in round glass coverslips (Knittel glass) in 4-well plates (Thermo Scientific) at a density of 1.5 x 10^4 cells per well. After 24 h media was replaced with Fe_3O_4@SiO_2 core-shell nanoparticles (synthesized via normal reverse microemulsion method) incubation solutions at 100, 50, 10 and 5 μg/mL in complete medium. Cultures were incubated in the above-mentioned conditions for 3 h. Afterwards, cell cultures were washed twice with a 0.1 M cacodylate buffer (TAAB) and fixed with a 2.5% glutaradehyde (Merck) in 0.1 M cacodylate buffer solution for 45 min. Samples were then dehydrated through a series of increasingly graded of ethanol (Merck Millipore) incubations for 8 minutes (use 50%, 70% and 90% grade of ethanol once and 100% grade of ethanol twice). Finally, samples were incubated for 15 min with Hexamethyldisilazane (Electron Microscopy Sciences) after which the coverslips were removed from the 4-well plate, mounted onto SEM stubs and analysed using a scanning electron microscope (Carl Zeiss Merlin).

Fe_3O_4@SiO_2 NPs cytotoxicity evaluation by Methylthiazolyldiphenyl-tetrazolium-bromide (MTT) assay. For cytotoxicity assays, cells were seeded at a density of 1.5 x 10^4 cells/well in 24-well plates. After 24 h, cultures were exposed to solutions of Fe_3O_4@SiO_2 core-shell nanoparticles (synthesized via normal reverse

microemulsion method) in complete medium at 100, 50, 10 and 5 μg/mL for 3 h. After incubation time, media was removed and 500 µl of MTT working solution (0.1 mg/ml MTT diluted in complete medium) were added. Cultures were further incubated for 3 h until the formation of formazan crystals was observed under an inverted contrast phase microscope (Olympus IX71). Afterwards, the MTT solution was removed and cultures were dried at room temperature in the dark at least one day.

Before carrying out the measures of absorbance, 500 µl of Dimethylsulfoxide (DMSO, Sigma Aldrich) were added to each well. Three wells per plate containing DMSO were used as a blank. The absorbance at 550 nm was read in a Victor TM X3 Multilabel Plate Reader (Perkin Elmer)

4.1.4.3 Phantom MR imaging test

Phantom MR imaging were performed at 7 T horizontal MR scanner (Bruker Biospec 7T MRI). The concentrations of Fe in the different samples were calculated according to the results of TGA and SQUID test. The Fe_3O_4@SiO_2 core–shell nanoparticles were dispersed in a solution of 2% Pluronic F-127 for 30 min using a sonication bath (Nahita Model I 610/3). Dispersed nanocomposites were mixed with an equal volume of melted agar solution (3%, w/v in water at 90ºC) to achieve final Fe concentrations of samples synthesized from normal and microwave assistance reverse microemulsion method ranging from 0.5mM to 01.25mM in 1.5% agar in water.

4.1.5 Results and discussion

First, the association of Fe_3O_4@SiO_2 NPs with cells was confirmed through SEM. In Figure 4.6, the plasma membrane of a HeLa cell from a culture that has been exposed to a Fe_3O_4@SiO_2 core-shell nanoparticles with different concentrations in complete medium solution for 3 h was analysed via SEM. The nanoparticles could be spotted on top of the collapsed microvilli typical of this cell line. A positive association of the nanoparticles with HeLa cells was observed even at the lowest concentration, being the highest concentration the one that showed more particles associated to the plasma membrane. The number of the nanoparticles observed on the top of collapsed microvilli was decreased with the decreasing of the concentrations of nanoparticles.

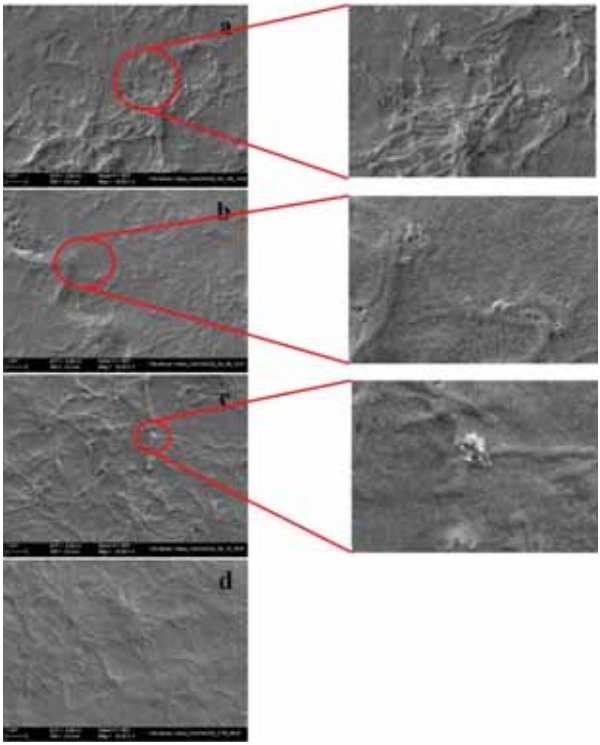

Figure 4.6 SEM image of the plasma membrane of a HeLa cell from a culture that has been exposed to a (a) 100 μg/mL, (b) 50μg/mL, (c) 10 μg/mL and (d) control group of Fe_3O_4@SiO_2 core-shell nanoparticles in complete medium solution for 3 h

After confirming the interaction of the nanoparticles with the cells, cytotoxicity evaluations via Methylthiazolyldiphenyl-tetrazolium-bromide (MTT) assay for Fe_3O_4@SiO_2 core-shell nanoparticles were carried out at different tested concentrations of nanoparticles. The results in Fig. 4.7 indicates that even at the highest concentration there are still 81% of cell remain alive

and the percentage of living cell was increased when the concentration of nanoparticles decreased. Considering that a percentage above 80% in viability is non-cytotoxic according to the Biological evaluation of medical devices, a preliminary conclusion can be made that the $Fe_3O_4@SiO_2$ core-shell nanoparticles have no cytotoxicity which can be attributed to the bio-compatible SiO_2 surface and relative small size of the core-shell nanoparticles.

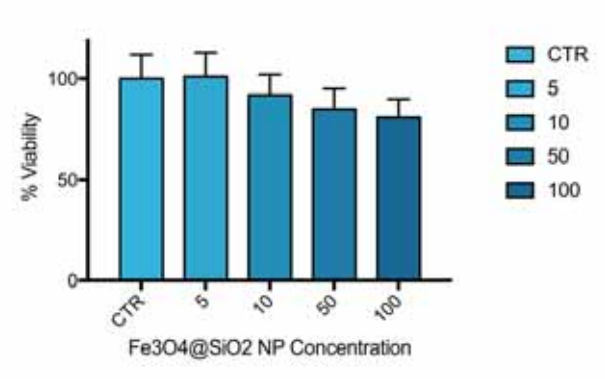

Figure 4.7 Bar graph depicting the viability results (in percentage) of each $Fe_3O_4@SiO_2$ core-shell nanoparticles tested concentration

Due to the magnetic nanocomposites show great potential as MRI contrast agents,[22, 23] relaxivity measurements of $Fe_3O_4@SiO_2$ core–shell nanoparticles were performed to evaluate their potential application as MRI contrast agents.

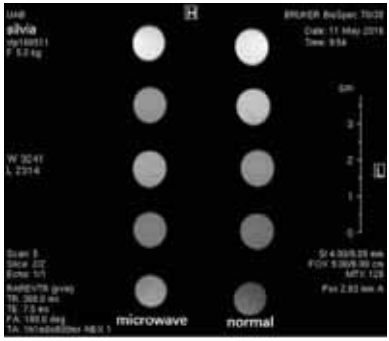

Figure 4.8 Phantom MR T_1 weighted image of Fe_3O_4@SiO_2 core–shell nanoparticles synthesized from normal and microwave assistance reverse microemulsion method

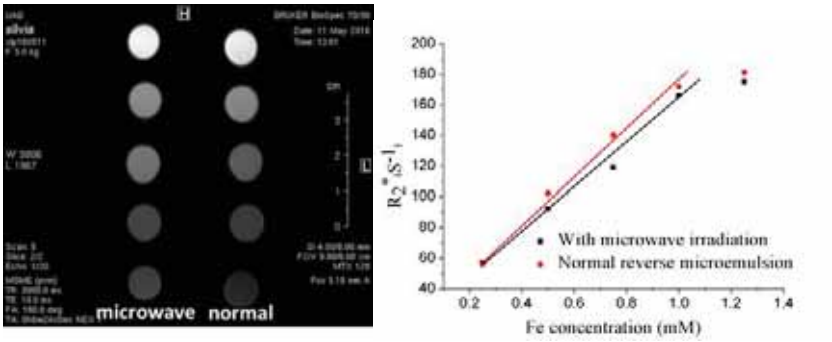

Figure 4.9 Phantom MR T_2 weighted image and R_2^* relaxation time analysis as a function of Fe concentration of Fe_3O_4@SiO_2 core–shell nanoparticles synthesized from normal and microwave assistance reverse microemulsion method

Figure 4.8 shows the T_1 weighted image of synthesized core-shell nanoparticles, both of them

didn't show clearly positive contrast enhancement effect, suggests that this kind of core-shell nanoparticles is not suitable for using as a T_1 weighted MRI contrast agent. In the meantime, Figure 4.9 shows the phantom MR T_2 weighted imaging of the samples, indicating negative contrast enhancement effect. This phenomenon can be explained by the existence of iron oxide nanoparticles, which can create strong inhomogeneity of magnetic field in the environment and therefore significantly enhance the transverse magnetization decays process. The relaxation times of these two nanocomposites were plotted versus the iron concentration, revealing their potential as negative contrast agents. The r_2^* relaxivities of Fe_3O_4@SiO_2 core–shell nanoparticles prepared by normal and microwave assistance reverse microemulsion method were calculated as $152 s^{-1}mM^{-1}$ and $148\ s^{-1}mM^{-1}$ respectively, which are nearly 47% of the value of commercial Endorem contrast agent ($325\ s^{-1}mM^{-1}$). The existence of SiO_2 shell hinders the interaction between magnetic nanoparticles and water molecules in the test media, which can actually result in the determination of lower r_2^*. Although the r_2^* relaxivities of Fe_3O_4@SiO_2 core–shell nanoparticles are lower than the commercial contrast agent, they are still applicable in MRI research and the biocompatible SiO_2 surface of these nanoparticles will make them easy to functionalize with biomolecules and other drugs indicating the promising application as multifunctional tools in biomedicine research.

4.1.6 Conclusion

The cytotoxicity of Fe_3O_4@SiO_2 core–shell nanoparticles prepared by normal and microwave assistance reverse microemulsion method was studied via SEM analysis of Hela cells interaction of nanoparticles and absorbance spectra measurement of MTT assay. The SEM study of plasma

membrane of a HeLa cell indicates a positive association of the nanoparticles with HeLa cells and the number of nanoparticles observed is proportional with the concentration of nanoparticles used in each culture media. The results of absorbance spectra measurement of MTT assay revealed that even at the highest concentration of nanoparticles, there still 81% of Hela cells remain alive. The results suggested that this kind of core-shell nanoparticles have no cytotoxicity. On the other hand, MRI properties of this kind of nanoparticles were evaluated through Phantom MR imaging test. The results indicate a strong negative contrast enhancement of this kind of core-shell nanoparticles. The r_2^* relaxivities of $Fe_3O_4@SiO_2$ core–shell nanoparticles were comparable with commercial contrast agent. The MRI results suggest that the synthesized core-shell nanoparticles have potential application as a T_2 weighted MRI contrast agent. The current findings will likely contribute to further application of $Fe_3O_4@SiO_2$ core–shell nanoparticles in biomedical research. For example, in application in vivo, non-cytotoxicity and ability to be imaged are the essential requirements, which need to be satisfied before doing experiments in living tissues or animals.

4.2 Fe_3O_4@SiO_2 core-shell nanoparticles functionalized with Merocyanine 540 (MC540) molecules

Merocyanine 540 (MC540) is a kind of anionic lipophilic dye, which can strongly bind to cell membranes. Until now MC540 has been used in biomedical research for photodynamic therapy[24-26] but the application of MC540 was limited by their tendency to aggregate forming dimers in aqueous solution[27, 28]. In this section, we explored a method to functionalize the Fe_3O_4@SiO_2 core-shell nanoparticles with MC540 molecules with less aggregation by taking the advantage of negatively charged SO_3^- group of MC540 molecules.

4.2.1 Synthetic process

4.2.1.1 Preparation of Fe_3O_4 nanoparticles

The oleic acid and oleylamine capped Fe_3O_4 nanoparticles were prepared through a modified way of the decomposition of iron oleate complex described in previous report.[21]

4.2.1.2 Synthesis of APTES functionalized Fe_3O_4@SiO_2 core-shell nanoparticles

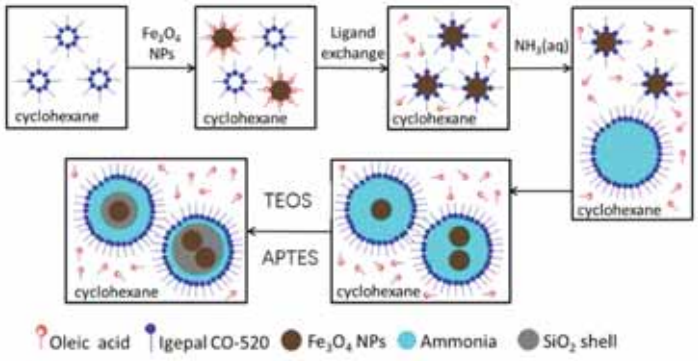

Figure 4.10 Schematic of synthesize Fe_3O_4@SiO_2-APTES core-shell nanoparticles

In this process, a modified method which was mentioned in the first paper[21] in chapter 3 was applied to synthesis Fe_3O_4@SiO_2-APTES core-shell nanoparticles. In typical experiments, 10ml of Igepal CO-520 (corresponding to 200 mM, in concentrations) were dissolved in 100ml cyclohexane and stirred for 30 min, then 0.61 ml of as prepared Fe_3O_4 (15.2mM) nanoparticles hexane solution was added into the solution and stirred for 3 h followed by adding a 2ml of ammonium hydroxide solution (corresponding to 280 mM concentration) into the solution and kept stirring for 1h to form a transparent water in oil (w/o) micro emulsion system. Finally the solution was mixed with 70µl of tetraethyl orthosilicate (TEOS) and kept stirring for 6h followed by adding 50µl of (3-Aminopropyl)triethoxysilane (APTES) and kept stirring for 18h. The solid was precipitated by adding ethanol and washed with ethanol through centrifugation (10000 rpm 10 min) for several times and finally the APTES functionalized Fe_3O_4@SiO_2 core-shell nanoparticles were dispersed in 40 ml ethanol. On the other hand, the synthesize Fe_3O_4@SiO_2

core-shell nanoparticles were also dispersed in 40 ml Tetrahydrofuran (THF) for further reaction to do the functionalization of MC540 in different solvent.

The concentration of the Fe_3O_4@SiO_2-APTES core-shell nanoparticles solution was decided through drying 1ml of the solution at 60℃ and measure the mass of the remaining solids. The final concentration is 1.5mg/ml.

4.2.1.3 Functionalization of Fe_3O_4@SiO_2-APTES core-shell nanoparticles with MC540 molecules

In this experiment, 20ml of obtained Fe_3O_4@SiO_2-APTES core-shell ethanol solution was mixed with 20ml ethanol followed by adding 3ml of MC540 aqueous solution (0.5mg/ml) and kept stirring overnight, noted as NPs-MC540-ethanol. On the other hand, 20ml of obtained Fe_3O_4@SiO_2-APTES core-shell ethanol solution was mixed with 20ml THF followed by adding 3ml of MC540 THF solution (0.5mg/ml) and kept stirring overnight, noted as NPs-MC540-THF. The solids were obtained through centrifugation (12000rpm, 20min) and dispersed in ethanol. The MC540 molecules were detected by UV-Vis analysis. TEM, FT-IR, SQUID and XRD techniques were also used to fully characterize the sample.

4.2.2 Results and discussion

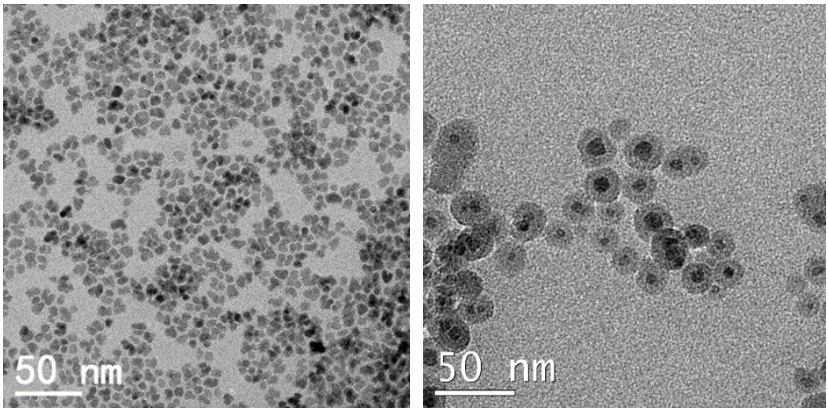

Figure 4.11 TEM images of Fe_3O_4 and Fe_3O_4@SiO_2-APTES core-shell nanoparticles

Figure 4.11 indicate that the synthesized Fe_3O_4 nanoparticles are highly dispersed in hexane with a narrow size distribution and the average diameter is about 8nm. After the formation of SiO_2 shell, the magnetite nanoparticles were fully covered with SiO_2 forming well-shaped core-shell nanoparticles with an average diameter around 30nm, and these core-shell nanoparticles are well dispersed in ethanol.

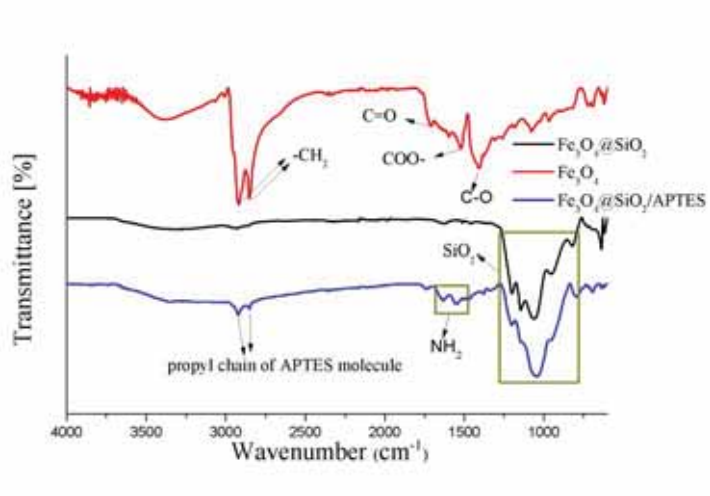

Figure 4.12 FT-IR curves of Fe_3O_4 nanoparticles, Fe_3O_4@SiO_2 core-shell nanoparticles and Fe_3O_4@SiO_2-APTES nanoparticles

In the FT-IR curve of Fe_3O_4 nanoparticles (Figure 4.12 red line), the absorption peaks at 2192 cm^{-1}, 2850 cm^{-1} are attributed to $–CH_2$ stretching vibration and 1708 cm^{-1} is coming from C=O stretching modes of COOH groups and the peaks at 1406 cm^{-1} could be ascribed to the coupling of hydroxyl bending vibration with C-O stretching vibration. The absorption band at 1598 cm^{-1} is the characteristic peak of C=C vibration and the peak at 1522 cm^{-1} can be attributed to COO^- asymmetric stretching vibration. All those peaks indicate that the oleic acid is absorbed on the Fe_3O_4 nanoparticles, which results in a well dispersion of Fe_3O_4 in hexane. After the microwave irradiation, the FT-IR curve of Fe_3O_4@SiO_2 (Figure 4.12 black line) shows two small peaks in 1512 cm^{-1}, 1457 cm^{-1} coming from stretching vibration of aromatic ring C=C and two strong peaks in 1200 cm^{-1} and 1060 cm^{-1} attributed to the symmetric and asymmetric stretching of

=C-O-C group. The existence of those vibration models indicates that there are still some amounts of Igepal CO520 attached on the nanoparticles' surface. The absorption bands at 1145 cm^{-1}, 953 cm^{-1}, 819 cm^{-1} are attributed to the vibration modes of SiO_2, which means that the SiO_2 successfully covered the Fe_3O_4 nanoparticles surface. The FT-IR results indicate the substitution of oleic acid and oleylamine capping ligands for the silica shell. Strong bands centered at 820 cm^{-1} can be unequivocally attributed to the vibration modes of SiO_2. In the Figure 4.12 blue line, the weak absorption peaks between 1490 cm^{-1} and 1631 cm^{-1} and at 3352 cm^{-1} attribute the NH_2 group of APTES and the peaks at 2922 cm^{-1} and 2852 cm^{-1} coming from the propyl chain of APTES molecule, all these peaks indicate the successful functionalization of -NH_2 group on the surface of core-shell nanoparticles.

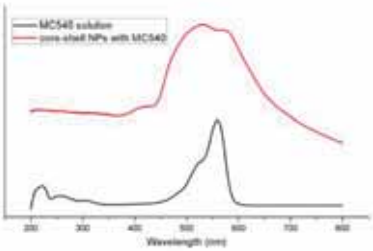

Figure 4.13 UV-Vis curves of MC540 aqueous solution and NPs-MC540-ethanol

In the UV-Vis test (Figure 4.13), both MC540 aqueous solution and NPs-MC540-ethanol samples show a strong absorption peaks around 540nm and 570nm which matches well with the absorption of dimers and monomers of MC540 molecules respectively and indicates the successfully decoration of MC540 on core-shell nanoparticles. The strong dimer-band can be

attributed to the polarity of ethanol solution.

It is essential to point out that the existence of dimer MC540 molecules has a negative effect on the phagocytoses process when the cells start interacting with nanoparticles and swallow them into the cells. In order to minimize this effect, the nanoparticles should be decorated with more monomer than dimer MC540 molecules.

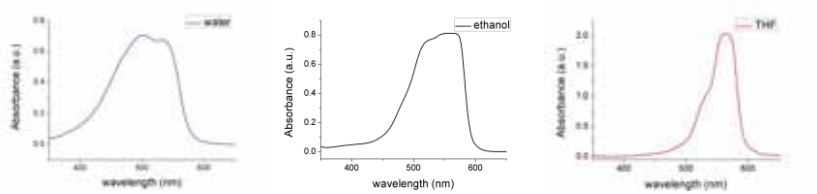

Figure 4.14 UV spectra curves of MC540 in different solvent (water, ethanol and THF)

In order to find the relationship between the bands distribution and the property of different solvents, a UV test was conducted in water, ethanol and THF (the polarity of solvent water>ethanol>THF). In Figure 4.14, the UV spectra curves of MC540 in different solvents were presented. It is very clearly that dye-monomer band increases linearly when the solvent polarity is decreased, the dimer-band is also decreased. This result is also identified with the previous report.[29]

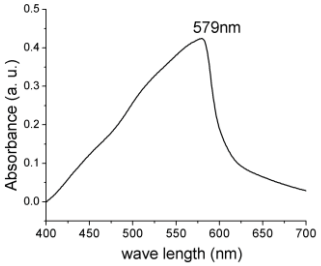

Figure 4.15 UV-vis curve of NPs-MC540-THF sample

In order to have the Fe3O4@SiO2-APTES core-shell nanoparticles decorated more monomers of MC540 molecules on the surface, THF were used as the solvent during the experiment (described in section 4.2.1.3). In the UV spectra result of the NPs-MC540-THF sample prepared in THF (Figure 4.15), a strong absorbance peak appeared at 579nm and there is no clear peak around 540nm. The result suggests that the MC540 molecules decorated on the Fe_3O_4@SiO_2-APTES core-shell nanoparticles surface are mainly monomer.

Figure 4.16 Photo images of (a) MC540 aqueous solution before decoration, (b) core-shell NPs aqueous solution before decoration, (c) core-shell NPs aqueous solution after decoration, (d) the reaction solution after decoration and the NPs-MC540-THF sample ethanol solution contact with an external magnet.

From the image above (Figure 4.16), the changing of the colour of reaction solutions is clearly observed. The pure MC540 aqueous solution (Figure 4.16 a) is red and the core-shell nanoparticles solution (Figure 4.16 b) is brown. After the decoration process, the nanoparticles were separated by centrifuge. The obtained solids were dispersed in water (Figure 4.16 c) and shown a red colour, while the remaining solution (Figure 4.16 d) shown a brown colour, which could be attributed to the ultra-stable core-shell nanoparticles in the solution. And the images also indicated the MC540 decorated core-shell nanoparticles could be easily separated by external magnet.

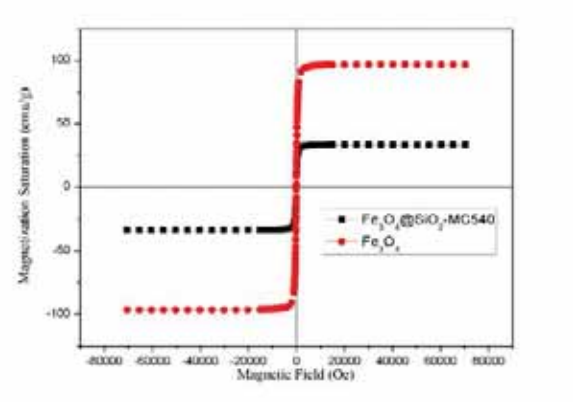

Figure 4.17 Field-dependent magnetization curves (5 K) for the prepared Fe_3O_4, Fe_3O_4@SiO_2-MC540 core-shell nanoparticles measured by SQUID

NPs-MC540-THF sample displays a strong magnetism that allows their separation from the solution with a magnet. Figure 4.17 shows the magnetization test of Fe_3O_4 and NPs-MC540-THF sample nanoparticles. Magnetite nanoparticles are superparamagnetic with a high saturation

magnetization value (96.9 emu/g). After covered by silica shell, the nanoparticles display a lower saturation magnetization (32.7 emu/g) but the core-shell structure remains superparamagnetic.

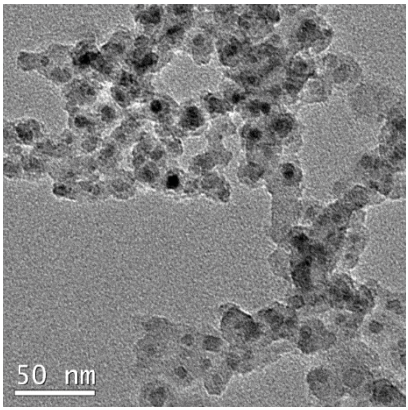

Figure 4.18 TEM image of NPs-MC540-THF sample nanoparticles

TEM image of NPs-MC540-THF sample nanoparticles (Figure 4.18) indicates that the nanoparticles are remaining core-shell structure but the aggregations are formed after the decoration of MC540. This can be attributed to the change of surface charge before and after the decoration process. But it could be an advantage for the application in magnetic manipulation since monodisperse Fe_3O_4@SiO_2 core-shell nanoparticles with small size are very difficult to separate via external magnetic field.

According the reference[24], the MC540 content in the core-shell was quantified by UV-Vis analysis and compared to a pre-determined standard curve. The loading efficiency in wt% was computed using Equation

$$\text{Photosensitizer loading } (\%) = \frac{\text{Mass of photosensitizers incorporated into particles}}{\text{Mass of particles}} * 100\%$$

The loading efficiency was calculated to 5%.

4.2.4 Conclusion

In this section, Fe_3O_4@SiO_2–MC540 core-shell nanoparticles are prepared by normal reverse microemulsion method. Two protocols were followed to decorate with MC540 molecules on the surface of nanoparticles, in ethanol and in THF. The UV-Vis results indicated that using both methods successfully decoration of MC540 molecules on core-shell nanoparticles take place. While the one in ethanol exhibit the formation of dimer compounds of MC540, on the other side Fe_3O_4@SiO_2–MC540 core-shell nanoparticles in THF represent high stability with more monomer of MC540, which suggests a promising process for avoiding the formation of MC540 dimer molecules (which are lack of affinity to the membrane) in the solution. The TEM image suggested the core-shell nanoparticles form small aggregations after the decoration process and the results of magnetic test indicate the NPs-MC540-THF sample nanoparticles can be manipulated via external magnetic field. The loading efficiency was calculated to 5% by the UV-vis results. This study would be helpful for the research in MC540 applications. By combining the advantage of magnetic core-shell nanoparticle with the photodynamic property and affinity to membranes of MC540, the synthesized Fe_3O_4@SiO_2–MC540 core-shell nanoparticles could provide us a promising tool in bio-imaging, photodynamic therapy and magnetic manipulation in bio-medical application.

4.3 Functionalization of Fe_3O_4@SiO_2 core-shell nanoparticles for the detection of L-thyroxine

4.3.1 Introduction

4.3.1.1 L-thyroxine and relative detection techniques

In human body, the thyroid hormones, triiodothyronine (T3) and L-thyroxine (T4), are derivatives of the thyroxine amino acid and synthesized in the thyroid gland. The thyroid hormones affect all the physiological process of our body for example metabolism, body temperature, growth and heart rate.[30] Among those thyroid hormones, thyroxine is very important since it constitutes around 93% of the metabolically active hormones secreted by gland. And the thyroxine can be classified into two forms, D-T4 and L-T4. The L-T4 has medical applications in the treatment of thyroid, promotes the metabolism in vivo and maintain the functions of the nervous system and cardiovascular system. A lower concentration of L-T4 would cause several diseases, such as hypothyroidisms, congenital hypothyroidism, and Beckwith syndrome in infants.[31, 32] Therefore, the detection of L-T4 in the blood has been proved very promising to analysis the thyroid status of our body.

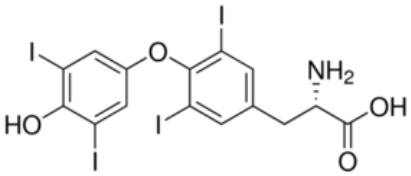

Figure 4.19 Molecule structure of L-thyroxine

To date, various techniques such as radioimmunoassay (RIA)[33], enzyme immunoassay[34], electrochemiluminescence[35], flow injection chemiluminescence[36], thin-layer chromatography[37] and gas chromatography mass spectroscopy (GC-MS)[37] have been widely used to determine thyroxine in the blood serum and urine samples but these methods were found not suitable for distinguish T4 isomers. On the other hand, these methods need expensive instruments and long time to set the test and the sensitivity of the test is not sufficient to determine the T4 status of patients.[38] While due to the relatively low cost of electrochemical sensing[39] and easier preparation, high sensitivity and selectivity of molecularly imprinted polymer (MIP) sensor[40], the combination of these two methods could have promising application in the detection of thyroxine.

4.3.1.2 Molecular imprinted polymer (MIP) sensor

Molecular imprinting technique is a template-assisted synthesis, which produces selective cavities in a 3D-polymeric network (Figure). Those cavities can be exposed via the elimination of the template, More interestingly, those exposed cavities not only fit the size and the shape of

the templates, but also occupy the interaction points (for example chemical bonds) to the respective template molecules.[41]

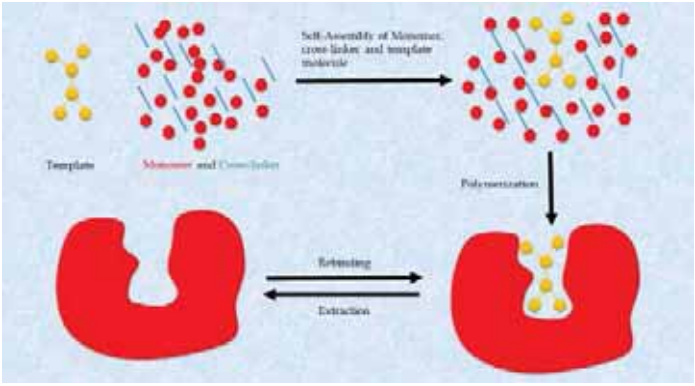

Figure 4.20 A schematic of molecularly imprinted polymer preparation steps [42]

In common with biosensors, MIP-base biosensors have been considered as promising candidate for future applications in food safety, environment sciences and biomedical sciences and numerous researches have been done in recent years. For example, Tingting Zhou et al. fabricated a selective and sensitive sensor based on MIP/acetylene black for the determination of azithromycin in pharmaceuticals applications[43], MIP-sensors were made based on chlorohemin modified molecularly imprinted microgel for the analysis of 2,4-dichiorophenol[44], Chien-Chong Hong et al. prepared a modified MIP film sensor with better molecular separation performance resulting to numerous applications in fluidic-based disposable biochips[45].

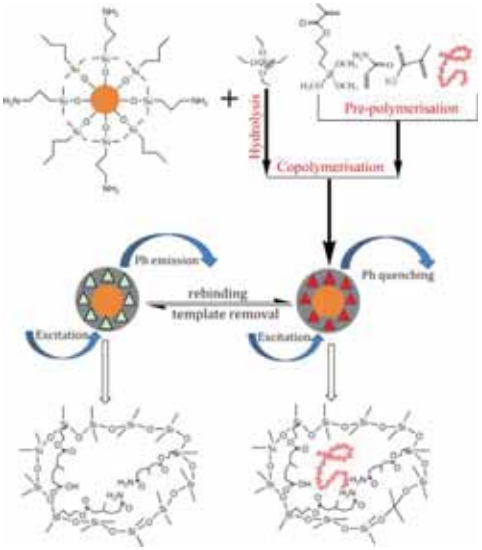

Figure 4.21 Schematic illustration of MIP Mn-doped ZnS QDs sensor for target proteins.[46]

In this chapter, organic molecules were imprinted on the surface of Fe_3O_4@SiO_2 core-shell nanoparticles. The obtained nanoparticles were used in the application of detecting L-thyroxine using electrochemistry method. The results of electrochemical test indicated a relatively high sensitivity than the MIP sensor made by large size Fe_3O_4@SiO_2 core-shell particles. The morphology analysis and BET test revealed the small size and large specific area of the nanoparticles, which can explain the reason of this high sensitivity. This study highlights one promising application of Fe_3O_4@SiO_2 core-shell nanoparticles in the field of bio-sensor technology.

4.3.2 Experimental process

4.3.2.1 Preparation of Fe_3O_4 nanoparticles

In this experiment, two kinds of Fe_3O_4 nanoparticles were synthesized, one is prepared via a similar process described in the first paper[21] in Chapter 3. Another kind of Fe_3O_4 particles was also synthesized by co-precipitation of a Fe^{2+}/Fe^{3+} mixed solution prepared from iron salts. In a typical experiment, 3.44 g of $FeCl_2 \cdot 4H_2O$ and 9.44 g of $FeCl_3 \cdot 6H_2O$ were dissolved in 160 mL of ultrapure water under nitrogen flow with magnetic stirring at 70-80ºC, then 60 mL of ammonia solution (Sigma 32%) were added drop by drop using a 25mL burette for 30-45 minutes to achieve a pH=9-10 units (measured by pH-meter) to obtain black precipitation. The black precipitation was then separated with the help of an external magnet and followed by gently washing with ultrapure water. The final product was dried at 60°C for 24 hours.

4.3.2.2 Preparation of $Fe_3O_4@SiO_2$ core-shell particles

In this process, two kinds $Fe_3O_4@SiO_2$ core-shell particles were synthesized. The $Fe_3O_4@SiO_2$ core-shell nanoparticles through the same process described in the first paper[21] in Chapter 3. This kind of particles were noted as $Fe_3O_4@SiO_2$ NPs.

In order to comparing the differences between the small size core-shell nanoparticles and large

size core-shell particles, the Fe_3O_4 nanoparticles obtain via coprecipitation method (described in section 4.3.2.2) were coated with amorphous SiO_2 layer with OH groups the surface for further reactions. In a typical process, 600 mg of Fe_3O_4 particles were dispersed in 80 mL of ethanol and 8 mL ultrapure water via ultrasonic treatment for 15 minutes in a round bottom flask of 250mL. After that, 10 mL of ammonia solution (Sigma 32%) and 4 mL of tetraethyl orthosilicate (Sigma reagent grade, 98%) were added into the solution. The mixture was kept stirring for 12 hours with an HEDOLPH® agitator. Then, the product was separated with an external magnet and washed with ultrapure water. This kind of particles were noted as Fe_3O_4@SiO_2 Ps.

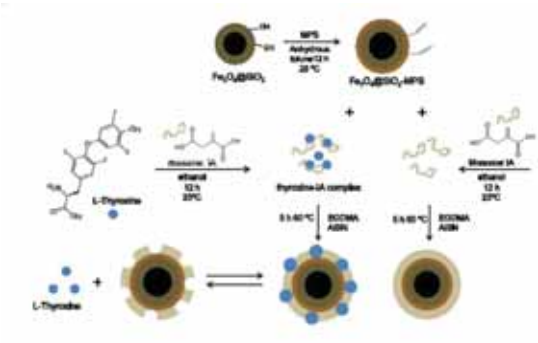

Figure 4.22 Scheme of preparation of Fe_3O_4@SiO_2-MIP and Fe_3O_4@SiO_2-NIP particles

4.3.2.3 Preparation of Fe_3O_4@SiO_2-MPS particles

In this experiment, the Fe_3O_4@SiO_2 NPs and Fe_3O_4@SiO_2 Ps synthesized in section 4.3.2.3 were further functionalized with 3-methacryloxypropyltrimethyloxysilane (MPS) which with an

acrylic group containing silanizating agent, to provide activated C=C groups for further copolymerization in the following step. In standard reactions, 500 mg of the pre-synthesized Fe_3O_4@SiO_2 NPs and Fe_3O_4@SiO_2 Ps were dispersed in 100 mL of anhydrous toluene in a three-neck round bottom flask respectively followed by adding 10 mL of MPS. Reactions were hold for 12 hours under nitrogen protection. The particles were separated with the help of magnet and gently washed with pure water. Then the product is dried at 60℃ for 24 hours and marked as Fe_3O_4@SiO_2-MPS NPs and Fe_3O_4@SiO_2-MPS Ps respectively.

4.3.2.4 Prepolymerization of the template L-thyroxine

Before the synthesis of the Fe_3O_4@SiO_2-MIP nanomaterials with affinity towards L-thyroxine, a pre-polymerization step of is required. To do that, 0.2 mmol L-thyroxine and 0.8 mmol itaconic acid were dissolved in 30 mL of ethanol in a sealed round bottom flask under magnetic stirring for 12 hours at room temperature. Similarly, the non-imprinted polymer (NIP) was prepared without the presence of the L-thyroxine template molecules. During this step, non-covalent weak interactions between the template and the monomer, mainly hydrogen bonds, electrostatic and hydrophobic interactions are formed maintaining a complex between L-thyroxine and itaconic acid.

4.3.2.5 Polymerization

During this step, 200 mg of Fe_3O_4@SiO_2-MPS NPs were mixed with pre-polymerization mixtures of MIP and NIP (prepared in section 4.3.2.5) respectively and kept stirring for 3 hours. After that, 4.0mmol of ethylene glycol dimetacrylate (EGDMA, Sigma) and 0.05mmoL of radical initiator (AIBN) were added and then the mixtures were treated with ultrasounds in a water bath for 5 minutes followed by purging with nitrogen to avoid the reaction with oxygen. Finally, the mixtures were heated to 60C° and hold for 5 hours under the mechanical stirring and nitrogen protection. The samples were marked as MIP-NPs and NIP-NPs.

4.3.2.6 Washing and template removing steps

Same procedure was applied in the case of MIP-NPs samples for washing and removing L-thyroxine template. The L-thyroxine extraction was done using a soxhlet extraction by using a mixture of methanol and acetic acid ($V_{methanol}$:$V_{acetic\ acid}$=9:1) as extracting solvent. The solution was changed every 12 hours during five days in order to remove L-thyroxine completely from particles surface. After that the product was dried at room temperature. L-thyroxine was considered totally eliminated when no analyte was detected in the eluent by spectrophotometry at 300 nm.

4.3.2.7 Determination of L-thyroxine by preconcentrating on MIP-NPs and direct electrochemical detection via cyclic voltammetry on m-GEC electrodes

A three-electrode setup was used for the electrochemical measurements, which comprises a double junction Ag/AgCl (Nº 900200, ORION Fisher Scientific) reference electrode with a saturated internal reference AgCl solution (Nº 900002, ORION Fisher Scientific) and an external reference solution of 10 % KNO_3 (Nº 900003, ORION Fisher Scientific), a platinum auxiliary electrode (Nº. 52-67, CRISON, Spain), and a working electrode (GEC or m-GEC). The cyclic voltammetry and other electrochemical characterization were performed with a potentiostat/galvanostat system Autolab PGSTAT10 (Eco Chimie, The Netherlands).

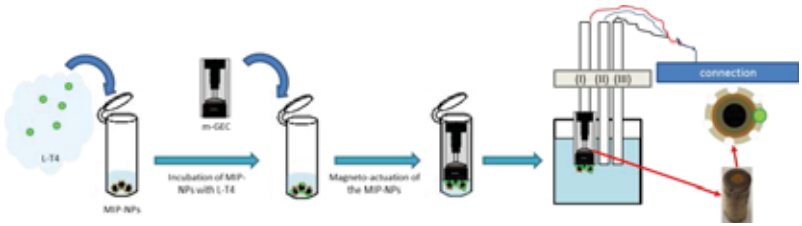

Figure 4.23 Scheme of the m-GEC electrodes set up

For this strategy, the protocol consists of the following steps:

1. Preconcentrating of the T4 on MIP-NPs: In this step, 100 μL of MIP-NPs citrate buffer (pH=7) suspension (5.5mg/mL) and 100μL of L-thyroxine aqueous solution ($5 \cdot 10^{-4}$ mol/L) were mixed in 2 mL eppendorf tubes, then shaking it at room temperature for 30 min. After that, the solids were separated with an external magnet and washed with Milli-Q water to remove the supernatant.

2. Magneto-actuation of the MIP-NPs on the surface of the m-GEC electrodes: In this step, the washed solids were resuspended in a volume of 180 μL citrate buffer and captured by the m-GEC electrode simply by dipping the electrode on the incubation tube.

3. Direct electrochemical detection by cyclic voltammetry in 20 mL HCl aqueous solution (pH=0.10). As a negative control, the NIP-NPs were test with the same method.

4.3.3 Results and Discussion

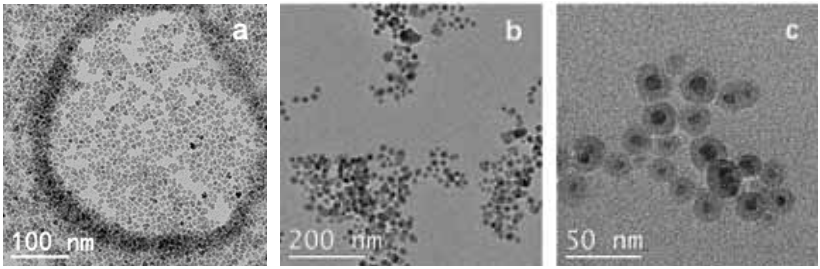

Figure 4.24 TEM images of synthesized (a) Fe_3O_4 nanoparticles and (b, c) Fe_3O_4@SiO_2 core-shell nanoparticles

As shown in the TEM images (Figure 4.24), the synthesized Fe_3O_4 nanoparticles were monodispersed in hexane with average diameter around 8nm. After the coating of SiO_2 layer, the Fe_3O_4@SiO_2 core-shell nanoparticles were formed and well dispersed in ethanol. The high resolution of Fe_3O_4@SiO_2 core-shell nanoparticles indicates the clearly existence of SiO_2 shell with the thickness of 7nm.

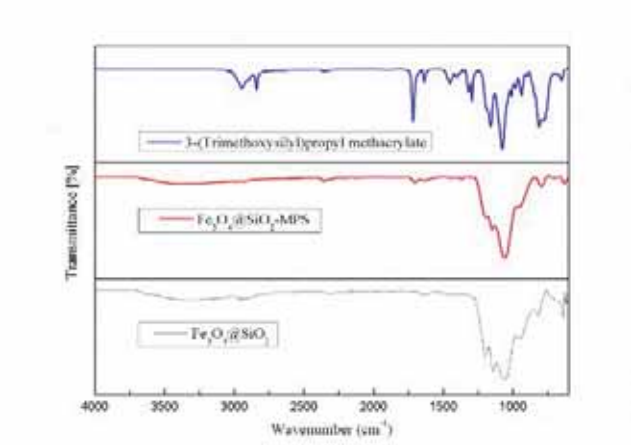

Figure 4.25 FT-IR spectra curves of 3-(Trimethoxysilyl)propyl methacrylate molecules, Fe_3O_4@SiO_2 core-shell nanoparticles and 3-(Trimethoxysilyl)propyl methacrylate decorated Fe_3O_4@SiO_2 core-shell nanoparticles

The infrared spectra (Figure 4.25) of the synthesized MPS decorated and non-MPS decorated Fe_3O_4@SiO_2 core-shell nanoparticles were recorded and compared to confirm the successfully functionalization of MPS molecules. A standard FT-IR spectra test was also done for pure MPS molecules for a reference. In the FT-IR spectra of pure MPS molecules, the strong absorption

band at 1717cm^{-1} can be attributed to the vibration of C=C bond and the absorption band at 1637cm^{-1} can be attributed to the vibration of C=O bond, these bands are the characteristic bands of MPS molecules. In the FT-IR spectra of MPS decorated F_3O_4@SiO_2 core shell nanoparticles two weak absorption bands at 1703 and 1639cm^{-1} are observed these bands don't appear in the non-MPS fuctionalized nanoparticles These two bands can be ascribed to the vibration of C=O and C=C bands and indicate the successfully functionalization of MPS on the surface of core-shell nanoparticles. The functionalization of MPS molecules on the surface of nanoparticles will provide us the C=C bands for further copolymerization with itaconic acid for the decoration of L-thyroxine molecules.

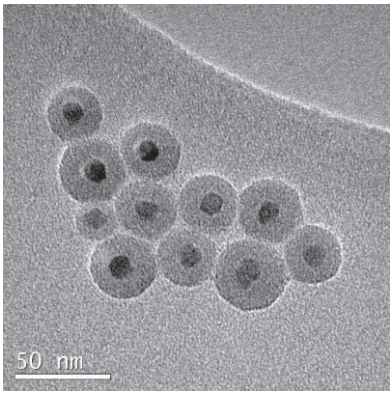

Figure 4.26 TEM images of Fe_3O_4@SiO_2-MPS NPs

From the TEM images of MPS decorated core-shell nanoparticles (Figure 4.26), the Fe_3O_4@SiO_2-MPS NPs still remain monodisperse with an average diameter around 30nm and very well dispersed in ethanol.

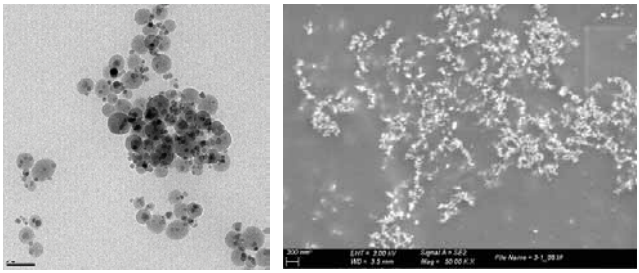

Figure 4.27 TEM and SEM image of MIP-NPs

The morphology analysis of synthesized MIP-NPs was carried out via TEM and SEM. The TEM result in Figure 4.27 indicates that the nanoparticles tend to form some small aggregations but the majority of them are still monodisperse. The SEM image in Figure 4.27 shows the existence of small aggregations with average size around 200nm and there are still single nanoparticles remaining on the graphite substrate, these results are identified with the information coming from TEM test. The formation of aggregation can be attributed to the polymerization of itaconic acid.

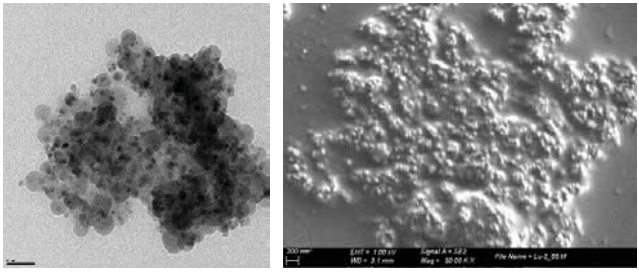

Figure 4.28 TEM and SEM image of MIP-NPs after washing process

After washing process, as shown in TEM image (Figure 4.28), bigger aggregates are formed

compared with the sample before washing process. The SEM image also indicate the presence of aggregates. The formation of those aggregates can be attributed to the drying process of the samples. The results of BET indicate the S_{BET}= 80m^2/g, while the theoretical surface area value of this kind of nanoparticles is around 200m^2. Since the BET test also requires a dried sample for the test, the drying process could be the main reason for the formation of aggregates.

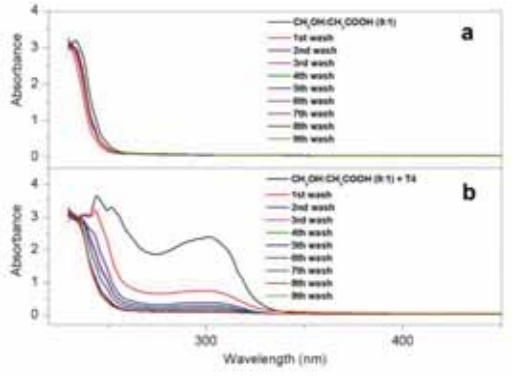

Figure 4.29 UV-Vis spectra of the solution after washing (a) the NIP-NPs and (b) MIP-NPs

In the UV-vis curves of the washing solution for NIP-NPs (Figure 4.29 a), any absorbance peak appeared. Instead, in the washing solution for MIP-NPs (Figure 4.29 b) there is a strong absorbance peak at 300nm which can be attributed to the presence of L-thyroxine, indicating the successfully decoration of template L-thyroxine. On the other hand, the UV-Vis from the washing solution for MIP-NPs (Figure 4.29 b) suggestes that the strength of the absorbance peak of L-thyroxine decreased with the time of the washing procedure and completely disappeared after 9 times of washing process, this phenomenon reveals that the decorated L-thyroxine was totally removed from the core-shell nanoparticles.

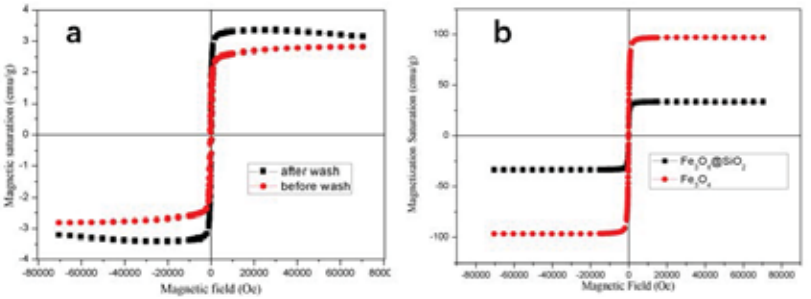

Figure 4.30 SQUID test of (a) MIP-NPs before and after washing process and (b) Fe_3O_4 and $Fe_3O_4@SiO_2$ nanoparticles

In Figure 4.32 are presented the results of SQUID test of MIP-NPs before and after washing process and Fe_3O_4 and $Fe_3O_4@SiO_2$ nanoparticles. Figure 4.30 (a) indicates that the magnetic saturation value increased after the washing process which can be attributed to the elimination of the non-magnetic template L-thyroxine molecules decreasing the total amount of mass in the nanoparticles. These results are in aggreement with the UV-Vis spectra in Figure 4.29. On the other side, when compared with the magnetic saturation of Fe_3O_4 (96.9 emu/g) and $Fe_3O_4@SiO_2$ (32.7 emu/g) nanoparticles (Figure 4.30 b), it is worth to note that the value of MIP-NPs (2.8 emug/g before washing and 3.3 emu/g after washing) is relatively low, this can be explained by the mass effect of the non-magnetic polymer and template L-thyroxine but the MIP-NPs remain superparamagnetic.

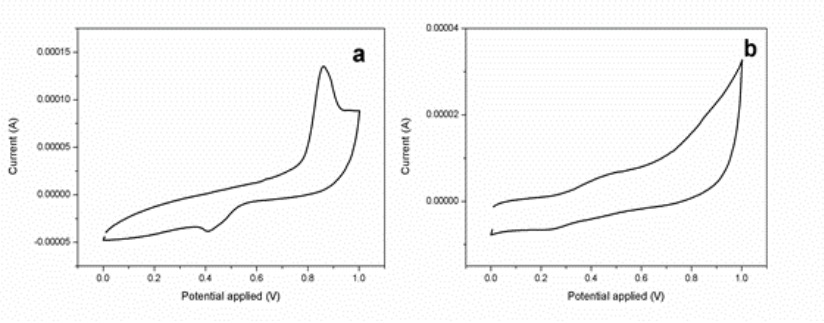

Figure 4.31 Cyclic voltammograms of m-GEC electrodes attached with L-thyroxine preconcentrated (a) MIP-NPs and (b) NIP-NPs

The cyclic voltammograms of the m-GEC electrodes attached with nanoparticles are presented in Figure 4.31. The electrodes were first immersed into a solution containing L-thyroxine. During the previous washing treatment, the L-thyroxine molecules were completely removed from the MIP nanoparticles and their respective cavities formed on the surface. These cavities will allow the L-thyroxine molecules in the test solution rebind on the surface of core-shell nanoparticles. When the m-GEC electrodes were transferred to HCl aqueous solution (pH=0.1) and tested by cyclic voltammetry, a signal of L-thyroxine appeared. The strong current peak is showed in CV of m-GEC electrodes attached with MIP-NPs, while there is no current peak exist in the CV curve of m-GEC electrodes attached with NIP-NPs. These results indicate the MIP-NPs were successfully prepared with nice ability for the detection of L-thyroxine in the solution.

4.3.4 Conclusion

In this section. Fe_3O_4@SiO_2 core-shell nanoparticles were prepared and used in the application of detection L-thyroxine. The synthesized core-shell nanoparticles were first successfully decorated with MPS molecules and followed by a uniform MIP layer on the surface of core-shell nanoparticles. The UV spetra and SQUID test results indicated the existence of L-thyroxine templates. The SEM and TEM images of synthesized MIP-NPs revealed the formation of aggregates. The electrochemistry results suggest the ability of this MIP-NPs to be suitable for the application in the dection of L-thyroxine. These results provide us the possibilty of using this core-shell nanoparticles in biosensor research area.

References

1. X. Wu, Y. Zhang, K. Takle, O. Bilsel, Z. Li, H. Lee, Z. Zhang, D. Li, W. Fan, C. Duan, E. M. Chan, C. Lois, Y. Xiang and G. Han, *ACS Nano*, 2016, **10**, 1060-1066.
2. D.-H. Park, J.-E. Kim, J.-M. Oh, Y.-G. Shul and J.-H. Choy, *Journal of the American Chemical Society*, 2010, **132**, 16735-16736.
3. D. Shao, X. Zhang, W. Liu, F. Zhang, X. Zheng, P. Qiao, J. Li, W.-f. Dong and L. Chen, *ACS Applied Materials & Interfaces*, 2016, **8**, 4303-4308.
4. W. Wu, T. Zhou, A. Berliner, P. Banerjee and S. Zhou, *Chemistry of Materials*, 2010, **22**, 1966-1976.
5. B.-T. Doan, S. Meme and J.-C. Beloeil, in *The Chemistry of Contrast Agents in Medical Magnetic Resonance Imaging*, John Wiley & Sons, Ltd, 2013, pp. 1-23.
6. J. O. Barentsz, F. M. J. Debruyne and S. H. J. Ruijs, in *Magnetic Resonance Imaging of Carcinoma of the Urinary Bladder*, Springer Netherlands, Dordrecht, 1990, pp. 13-27.
7. W. R. Hendee and E. R. Ritenour, in *Medical Imaging Physics*, John Wiley & Sons, Inc., 2003, pp. 367-388.
8. J. Smith, in *Imaging and Technology in Urology: Principles and Clinical Applications*, eds.

S. Payne, I. Eardley and K. O'Flynn, Springer London, London, 2012, pp. 61-65.

9. A. Leroy-Willig and D. Geldwerth-Feniger, in *Textbook of in vivo Imaging in Vertebrates*, John Wiley & Sons, Ltd, 2007, pp. 1-56.
10. D. Sappey-Marinier and A. Briguet, in *Medical Imaging Based on Magnetic Fields and Ultrasounds*, John Wiley & Sons, Inc., 2014, pp. 73-262.
11. R. Deichmann, in *fMRI Techniques and Protocols*, ed. M. Filippi, Humana Press, Totowa, NJ, 2009, pp. 3-29.
12. D. Bergin and D. G. Mitchell, in *Textbook of Gastroenterology*, Blackwell Publishing Ltd., 2009, pp. 3173-3211.
13. B. Tomanek and J. C. Sharp, in *Biomedical Imaging*, John Wiley & Sons, Inc., 2012, pp. 131-179.
14. J. P. Ridgway, *Journal of Cardiovascular Magnetic Resonance*, 2010, **12**, 71.
15. P. A. Boulby and F. J. Rugg–Gunn, in *Quantitative MRI of the Brain*, John Wiley & Sons, Ltd, 2004, pp. 143-201.
16. É. Tóth, L. Helm and A. E. Merbach, in *Comprehensive Coordination Chemistry II*, ed. T. J. Meyer, Pergamon, Oxford, 2003, pp. 841-881.
17. P. Tyler and S. Butt, in *Radionuclide and Hybrid Bone Imaging*, eds. I. Fogelman, G. Gnanasegaran and H. van der Wall, Springer Berlin Heidelberg, Berlin, Heidelberg, 2012, pp. 149-171.
18. C. S. Bonnet and É. Tóth, in *Ligand Design in Medicinal Inorganic Chemistry*, John Wiley & Sons, Ltd, 2014, pp. 321-354.
19. S. Namkung, C. J. Zech, T. Helmberger, M. F. Reiser and S. O. Schoenberg, *Journal of Magnetic Resonance Imaging*, 2007, **25**, 755-765.
20. D. D. Schwert, J. A. Davies and N. Richardson, in *Contrast Agents I: Magnetic Resonance Imaging*, ed. W. Krause, Springer Berlin Heidelberg, Berlin, Heidelberg, 2002, pp. 165-199.
21. C. Y. Lu, T. Puig, X. Obradors, S. Ricart and J. Ros, *RSC Advances*, 2016, **6**, 88762-88769.
22. Q. L. Vuong, J. F. Berret, J. Fresnais, Y. Gossuin and O. Sandre, *Advanced healthcare materials*, 2012, **1**, 502-512.
23. L. Sandiford, A. Phinikaridou, A. Protti, L. K. Meszaros, X. Cui, Y. Yan, G. Frodsham, P. A.

Williamson, N. Gaddum and R. M. Botnar, *Acs Nano*, 2012, **7**, 500-512.

24. H. Chen, G. D. Wang, Y.-J. Chuang, Z. Zhen, X. Chen, P. Biddinger, Z. Hao, F. Liu, B. Shen, Z. Pan and J. Xie, *Nano Letters*, 2015, **15**, 2249-2256.
25. N. M. Idris, M. K. Gnanasammandhan, J. Zhang, P. C. Ho, R. Mahendran and Y. Zhang, *Nat Med*, 2012, **18**, 1580-1585.
26. H. Wang, Z. Liu, S. Wang, C. Dong, X. Gong, P. Zhao and J. Chang, *ACS Applied Materials & Interfaces*, 2014, **6**, 3219-3225.
27. P. K. Gupta, K. Das and M. Sharma, *Procedia Engineering*, 2014, **92**, 9-18.
28. P. Kaschny and F. M. GoÑI, *European Journal of Biochemistry*, 1992, **207**, 1085-1091.
29. P. I. Lelkes and I. R. Miller, *The Journal of Membrane Biology*, 1980, **52**, 1-15.
30. S. Chitravathi, B. Kumaraswamy, E. Niranjana, U. Chandra, G. Mamatha and B. Sherigara, *Int. J. Electrochem. Sci*, 2009, **4**, 223-237.
31. B. B. Prasad, M. P. Tiwari, R. Madhuri and P. S. Sharma, *Journal of Chromatography A*, 2010, **1217**, 4255-4266.
32. B. Oerbeck, K. Sundet, B. F. Kase and S. Heyerdahl, *Pediatrics*, 2003, **112**, 923-930.
33. D. Sun, X. Xie, Y. Cai, H. Zhang and K. Wu, *Analytica Chimica Acta*, 2007, **581**, 27-31.
34. K. Wu, H. Wang, F. Chen and S. Hu, *Bioelectrochemistry*, 2006, **68**, 144-149.
35. A. Waseem, M. Yaqoob, A. Nabi and G. M. Greenway, *Analytical Letters*, 2007, **40**, 1071-1083.
36. E. Gök and S. Ateş, *Analytica Chimica Acta*, 2004, **505**, 125-127.
37. E. Rakov, in *Nanotubes and Nanofibers*, CRC Press, 2006, pp. 37-108.
38. W. Kangbing, J. Xiaobo, F. Junjie and H. Shengshui, *Nanotechnology*, 2004, **15**, 287.
39. C. Hu, Q. He, Q. Li and S. Hu, *Analytical Sciences*, 2004, **20**, 1049-1054.
40. B. B. Prasad, R. Madhuri, M. P. Tiwari and P. S. Sharma, *Analytica Chimica Acta*, 2010, **681**, 16-26.
41. L. Uzun and A. P. F. Turner, *Biosensors and Bioelectronics*, 2016, **76**, 131-144.
42. Z. O. Uygun, H. D. E. Uygun, N. Ermiş and E. Canbay, in *Biosensors - Micro and Nanoscale Applications*, ed. T. Rinken, InTech, Rijeka, 2015, p. Ch. 03.
43. T. Zhou, Y. Tao, H. Jin, B. Song, T. Jing, D. Luo, Y. Zhou, Y. Zhou, Y.-I. Lee and S. Mei,

PLOS ONE, 2016, **11**, e0147002.

44. J. Zhang, J. Lei, H. Ju and C. Wang, *Analytica Chimica Acta*, 2013, **786**, 16-21.
45. C.-C. Hong, C.-C. Lin, C.-L. Hong and P.-H. Chang, *Biomedical Microdevices*, 2012, **14**, 435-441.
46. L. Tan, C. Huang, R. Peng, Y. Tang and W. Li, *Biosensors and Bioelectronics*, 2014, **61**, 506-511.

Chapter 5 Conclusions

1. Fe_3O_4@SiO_2 core-shell nanoparticles were synthesized via normal and microwave assistance reverse microemulsion method. The morphology of the obtained core-shell nanoparticles can be manipulated through changing the parameters of the reaction. Thanks to the fast heating process of microwave irradiation, the microwave assistance reverse microemulsion method turns out to be a promising method to prepare nanomaterials.
2. The synthesized Fe_3O_4@SiO_2 core-shell nanoparticles were functionalized with APTES reactants to have -NH_2 groups on the surface. These nanoparticles were used as supports for silver nanoparticles catalysts. The obtained Fe_3O_4@SiO_2/Ag nanocomposites show excellent catalytic property in the in the reduction of 4-nitroaniline with highly reactivity and recyclability.
3. The Fe_3O_4 nanoparticles were synthesized inside CNTs via decomposition of iron precursor inside the cavities of CNTs. The synthesized nanoparticles were relatively smaller than those synthesized without the presence of CNTs, on the other side FeO phase was detected in the synthesized Fe_3O_4@CNTs nanocomposites indicate confinement and template effect of CNTs in the preparation of nanoparticles.
4. The Fe_3O_4@CNTs nanocomposites were further coated with SiO_2 to seal the synthesized Fe_3O_4 nanoparticles inside CNTs forming Fe_3O_4@CNTs@SiO_2

nanocapsules. The nanoparticles were successfully protected from leakage and corrosion even in a harsh environment. The obtained Fe_3O_4@CNTs nanocomposites and Fe_3O_4@CNTs@SiO_2 nanocapsules show good r_2^* relaxivities in MRI test, suggested potential application bio-imaging research.

5. The cytotoxic study indicated the synthesized Fe_3O_4@SiO_2 core-shell nanoparticles are non-cytotoxic. On the side, these nanoparticles also have good r_2^* relaxivities when used in the T_2 weighted MRI. Those results suggested potential application of Fe_3O_4@SiO_2 core-shell nanoparticles in biomedicine research.
6. The Fe_3O_4@SiO_2 core-shell nanoparticles were decorated with MC540 molecules in two different solvents. All of them indicate successfully decoration while the presence monomer and dimer compounds on the surface of nanoparticles can be controlled via changing the solvents.
7. MIP-biosensor was fabricated through decoration of the Fe_3O_4@SiO_2 core-shell nanoparticles with molecule imprinted polymers and L-thyroxine templates. By removing the templates from the nanoparticles, this kind of Fe_3O_4@SiO_2-MIP nanocomposites show nice property for detecting L-thyroxine indicate another promising application of Fe_3O_4@SiO_2 core-shell nanoparticles in biosensor research.

List of Figures

Notes

In this PhD thesis, the research work is focused on the synthesis and application magnetic nanomaterials:

1. Fe_3O_4@SiO_2 core-shell nanoparticles were prepared via reverse microemulsion method in two different ways and characterized with different techniques. The effects of reaction parameters on the morphology of final core-shell nanoparticles were studied.
2. Fe_3O_4@CNTs nanocomposites were synthesized by in-situ decomposition of Fe (acac)3 precursor inside CNTs. The obtained nanocomposites were further sealed with SiO_2 to prepare a novel Fe_3O_4@CNTs@SiO_2 nanocapsulates.
3. The MRI imaging property of synthesized Fe_3O_4@SiO_2 core-shell nanoparticles and Fe_3O_4@CNTs@SiO_2 nanocapsulates were studied, indicated their potential application in bio-imaging research.
4. Fe_3O_4@SiO_2 core-shell nanoparticles were decorate with Ag nanoparticles and used in the reaction of reduction of 4-nitroaniline. The results suggested that the Fe_3O_4@SiO_2/Ag nanocomposites occupy high catalytic efficiency and recycling property.
5. Different bio-molecules were used in the functionalization of Fe_3O_4@SiO_2 core-shell nanoparticles and their applications in bio-medicine area were studied.

Unforgettable memory with the amazing group and fascinating city, it will always be my great pleasure to live and study in UAB!